Research Square

Preprints are preliminary reports that have not undergone peer review.
They should not be considered conclusive, used to inform clinical practice,
or referenced by the media as validated information.

# Targeting a novel liver-bone communication by SIRT2 for osteoporosis treatment

**longshuai lin**
Department of Orthopedics, Shanghai General Hospital, Shanghai Jiaotong University School of Medicine

**Zengya Guo**
Department of General Surgery, Shanghai General Hospital, Shanghai Jiao Tong University School of Medicine

**Enjun He**
Department of Orthopedics, Shanghai General Hospital, Shanghai Jiaotong University School of Medicine

**Difei Wang**
Department of Pathophysiology, Key Laboratory of Cell Differentiation and Apoptosis of Ministry of Education, Shanghai Jiao Tong University School of Medicine

**Yingting Zhang**
Department of Pathophysiology, Key Laboratory of Cell Differentiation and Apoptosis of Ministry of Education, Shanghai Jiao Tong University School of Medicine

**weihong Guo**
Department of Orthopedics, Shanghai General Hospital, Shanghai Jiaotong University School of Medicine

**qian wei**
Department of Pathophysiology, Key Laboratory of Cell Differentiation and Apoptosis of Ministry of Education, Shanghai Jiao Tong University School of Medicine

**Jingchi Li**
Department of Pathophysiology, Key Laboratory of Cell Differentiation and Apoptosis of Ministry of Education, Shanghai Jiao Tong University School of Medicine

**lulu Wo**
Department of Pathophysiology, Key Laboratory of Cell Differentiation and Apoptosis of Ministry of Education, Shanghai Jiao Tong University School of Medicine

**Ming He** ( heming@shsmu.edu.cn )
Department of Pathophysiology, Key Laboratory of Cell Differentiation and Apoptosis of Ministry of Education

**Qinghua Zhao**
Department of Orthopedics, Shanghai General Hospital, Shanghai Jiaotong University School of Medicine

Article

**Keywords:** osteoporosis, aging, hepatocyte, SIRT2, LRG1, osteoclast differentiation, small extracellular vesicles (sEVs)

**Posted Date:** May 11th, 2022

**DOI:** https://doi.org/10.21203/rs.3.rs-1628032/v1

**License:** This work is licensed under a Creative Commons Attribution 4.0 International License.
Read Full License

# Title: Targeting a novel liver-bone communication by SIRT2 for osteoporosis treatment

Longshuai Lin[1,2], Zengya Guo[3], Enjun He[2], Difei Wang[1], Yingting Zhang[1], Weihong Guo[2], Qian Wei[1], Jingchi Li[1], Lulu Wo[1], Ming He[1*], Qinghua Zhao[2*]

[1] Department of Pathophysiology, Key Laboratory of Cell Differentiation and Apoptosis of Ministry of Education, Shanghai Frontiers Science Center of Cellular Homeostasis and Human Diseases, Shanghai Jiao Tong University School of Medicine, Shanghai, China.

[2] Department of Orthopedics, Shanghai General Hospital, Shanghai Jiao Tong University School of Medicine, Shanghai, China.

[3] Department of General Surgery, Shanghai General Hospital, Shanghai Jiao Tong University School of Medicine, Shanghai, China.

*Corresponding author. E-mail: heming@shsmu.edu.cn (M.H); qinghua.zhao@shgh.cn (QH.Z).

## Abstract

The pathophysiologic role of liver in bone metabolism remains largely unknown. Here, we uncover a novel liver-bone axis regulated by hepatocyte SIRT2. We firstly demonstrated that liver-specific SIRT2 deficiency (*SIRT2*-KO$^{hep}$) obviously inhibits osteoclastogenesis and alleviates osteoporosis in aged and postmenopausal osteoporosis mouse models. Mechanistically, leucine-rich alpha-2-glycoprotein 1 (LRG1) was identified as the functional cargo in hepatocyte-derived small extracellular vesicles (sEVs), which is required for the protection of *SIRT2*-KO$^{hep}$ against osteoclastogenesis. In hepatocytes, *SIRT2*-KO$^{hep}$ up-regulates the expression of LRG1 in hepatocyte-derived sEVs (sEVs-LRG1) through increasing acetylation of H4K16. The sEVs-LRG1 is transfered to bone marrow-derived

monocytes (BMDMs) to suppress osteoclast differentiation through directly inhibiting nuclear translocation of NF-κB p65. Therapeutically, treating ovariectomized mice with SIRT2 pharmacological inhibitor AGK2 or sEVs purified from LRG1-overexpressed AML12 hepatocytes obviously attenuated osteoclastogenesis and bone loss. In accordance, sEVs derived from either human LRG1$^{high}$ plasma or hepatocytes with SIRT2 inhibition may markedly inhibit human osteoclast differentiation. Importantly, the clinical data showed that the plasma sEVs-LRG1 was positively correlated with bone mineral density and negatively related with bone resorption marker in patients. Therefore, drugs targeting the hepatocyte-osteoclast communication, including hepatocyte SIRT2 and sEVs-LRG1, should be considered as promising therapeutic strategy for primary osteoporosis.

**Keywords**: osteoporosis, aging, hepatocyte, SIRT2, LRG1, osteoclast differentiation, small extracellular vesicles (sEVs)

## Introduction

Osteoporosis is a common systemic skeletal disease characterized by altered bone metabolism, decreased bone mass, micro-architectural deterioration, and increased fragility fracture risk[1,2]. Bone metabolism is characterized by an intimate cooperation of bone cells including osteoblasts, osteoclasts, and osteocytes in order to maintain bone tissue quantity and the integrity of bone structure[2]. The disruption of the exquisite balance between bone resorption driven by osteoclasts and bone formation mediated by osteoblasts underlies the pathogenesis of osteoporosis[3]. Increasing age, especially postmenopausal female, is closely associated with the condition[2]. Osteoclasts are multinucleated bone-resorbing cells that differentiate from the

precursor cells, bone marrow-derived monocytes (BMDMs), in the presence of two indispensable cytokines: macrophage-colony stimulating factor (M-CSF) and receptor activator of nuclear factor (NF)-κB ligand (RANKL)[4]. Among them, NF-κB, comprised of several subunits such as p50, p52, and p65, is an important downstream transcription factor of the RANKL-RANK signaling pathway. Moreover, RANKL-induced NF-κB p65 activation and nuclear translocation are important for the initial induction of nuclear factor of activated T-cells cytoplasmic 1 (NFATc1), which is a master regulator of osteoclast differentiation and induces the expression of downstream osteoclast-specific genes, such as those coding for tartrate-resistant acid phosphatase (TRAP), Cathepsin K (CTSK), dendritic cell-specific transmembrane protein (DC-stamp) and osteoclast-associated receptor (OSCAR)[5-7]. Therefore, preventing osteoclast activation, especially negatively regulating NF-κB-NFATc1, is one way to treat osteoporosis in clinics.

Meanwhile, osteoporosis is a systemic bone disease. Besides the intimate cooperation of bone cells, bone metabolism is regulated by the complex communication between bone cells and other organs, providing new insights for osteoporosis therapy[8,9]. Liver is a dynamic organ in many physiological and pathological processes, including the regulation of systemic glucose, lipid and Vitamin D (VitD) metabolism[10,11]. Almost all patients with chronic liver disease (CLD) show altered bone metabolism and almost 75% of patients with CLD sooner or later suffer from severe osteoporosis, suggesting liver plays a pivotal role in regulating bone remodeling[12]. However, little has been reported about the roles of liver in primary osteoporosis, especially the most frequent senile osteoporosis and postmenopausal osteoporosis. Though there are some proteins secreted by liver involves bone metabolism[13], alterations of VitD metabolism is the

most studied liver-bone communication contributor to primary osteoporosis as VitD is hydroxylated by VitD 25-hydroxylase (CYP2R1) and sterol27-hydroxylase (CYP27A1) in liver[12]. However, VitD supplementation alone is not sufficient to prevent or delay loss of bone mineral densities (BMD) in patients with osteoporosis. These studies suggest the other unknown liver-bone communications are crucial and required for the pathogenesis and development primary osteoporosis.

Small extracellular vesicles (sEVs) may be produced by diverse cells and function as important cell-cell messengers[14]. Hepatocytes are sEVs-releasing and/or sEVs-targeted cells. Moreover, heptocyte-derived sEVs are released under either physiologic or pathologic conditions, including aging and liver diseases, and exert a wide range of effects on target cells by transmitting hepatocyte-associated protein cargo as well as mRNA, miRNA, and lipids[15]. To bone, sEVs involve in the communication among bone cells in the field of bone remodeling predominantly by paracrine effect[16]. Recent studies have detected that osteoblast-derived sEVs could fuse with osteoclasts to promote osteoclastogenesis and boost the clearance of damaged tissue during bone remodeling[17]. However, the pathophysiologic effects of hepatocyte-derived sEVs in bone remodeling, especially osteoblastogenesis and osteoclastogenesis, have so far not been described.

Sirtuin 2 (SIRT2) is a nicotinamide adenine dinucleotide ($NAD^+$)-dependent protein deacetylase and the only sirtuin mainly located in the cytoplasm and abundantly expressed in the liver[18]. Accumulating studies have found that SIRT2 plays an important role in the regulation of life activities such as aging, metabolism, apoptosis, cell differentiation, cell cycle, inflammation, and tumorgenesis. However, SIRT2 plays controversy and multiple roles by

deacetylating different substrates in diverse liver diseases, including alcoholic liver disease (ALD), nonalcoholic fatty liver disease (NAFLD), liver fibrosis and hepatic ischemia-reperfusion (I/R) injury[18]. Our previous work has demonstrated that SIRT2 in macrophages prevents aging-associated inflammation and maintains hepatic insulin sensitivity during physiological aging through deacetylaiton of NLRP3[19]. However, the contribution of SIRT2 in hepatocytes to bone homeostasis and osteoporosis is unknown.

Here, we uncovered a novel hepatocyte-osteoclast communication regulated by SIRT2 with therapeutic potential in osteoporosis. We demonstrated that liver-specific SIRT2 deficiency (*SIRT2*-KO$^{hep}$) obviously abolishes bone loss and osteoporosis in aged mice and ovariectomy (OVX)-induced postmenopausal osteoporosis mouse model. We elucidated the mechanism in vitro and in vivo that *SIRT2*-KO$^{hep}$-upregulated leucine-rich alpha-2-glycoprotein 1 (LRG1) in hepatocyte-derived sEVs (sEVs-LRG1) transfer via blood to BMDMs to suppress osteoclastogenesis through inhibiting NF-κB p65 activation. Moreover, we show that AGK2, a specific inhibitor for SIRT2, and osteoclast-targeted sEVs-LRG1 treatment could repress the differentiation of osteoclasts from both OVX mice and human primary mononuclear cells. The clinical data further verified that plasma sEVs-LRG1 expression was strongly and positively correlated with BMD and negatively related with bone resorption marker in patients.

## Results

**Hepatocyte-specific SIRT2 deficiency prevents age-related bone loss by suppressing osteoclastogenesis in mice.** To investigate the role of hepatocyte SIRT2 in bone homeostasis

in vivo, we generated a liver-specific SIRT2-knockout mice using a floxed SIRT2 mouse strain and an Alb-Cre line as previously described[20]. Compared to the young *SIRT2*$^{flox/flox}$ Alb-Cre$^{-}$ (LoxP) control littermates (3 months old), the young *SIRT2*$^{flox/flox}$Alb-Cre$^{+}$ (*SIRT2*-KO$^{hep}$) mice were phenotypically unremarkable, including normal body weight and bone mass (Supplementary Fig. 1). With aging, the micro-CT (μCT) analysis of distal femur showed obvious bone loss and osteoporosis in both aged female and male mice (18 months old) (Fig. 1a-d). Surprisingly, compared with old LoxP mice, the old *SIRT2*-KO$^{hep}$ mice in both sexes exhibited markedly increased bone mass (Fig. 1a, c), shown by increased bone volume/tissue volume ratio (BV/TV), trabecular number (Tb.N), and decreased trabecular separation (Tb.Sp) (Fig. 1b, d). Trabecular thickness (Tb.Th) was not different between groups (Fig. 1b, d). These results suggest that genetic deletion of SIRT2 in hepatocyte significantly slows down bone loss and prevents senile osteoporosis in mice.

To examine whether SIRT2 deficiency in hepatocytes disrupted the dynamic balance between osteoclasts and osteoblasts, we measured the markers for bone resorption and bone formation. Compared with aged LoxP mice, there was obviously decreased level of serum C-terminal telopeptide for type 1 collagen (CTX-1) in aged *SIRT2*-KO$^{hep}$ mice, suggesting that *SIRT2*-KO$^{hep}$ abolishes bone resorption and osteoclast activity (Fig. 1e, g). Moreover, lower number of TRAP-positive osteoclasts shown by TRAP staining on the paraffin-embedded bone sections was observed on the surface of trabecular bone in the female (Fig. 1i, j) and male (Fig. 1k, l) *SIRT2*-KO$^{hep}$ old mice compared to LoxP group, which is consistent with the CTX-1 serological evidence. Meanwhile, we noted the similar level of serum procollagen type 1 N-propeptide (P1NP) (Fig. 1f, h) and number of osteoblasts (Supplementary Fig. 2) between aged

groups, which suggests similar bone formation and osteoblast activity. In sum, these results provide evidence that *SIRT2*-KO$^{hep}$ prevents age-related osteoporosis by suppressing osteoclastogenesis.

**SIRT2$^{-/-}$ hepatocyte-derived sEVs abolish osteoclastogenesis.** To investigate the molecular mechanisms underlying the novel liver-bone communication by SIRT2 in senile osteoporosis, we firstly verify the effect of the plasma from two aged mouse groups on osteoblast and osteoclast differentiation. For osteoblast differentiation, bone marrow-derived mesenchymal stem cells (BM-MSCs) from C57BL/6 mice were isolated and cultured with the plasma of aged LoxP or *SIRT2*-KO$^{hep}$ male mice (LoxP-plasma or *SIRT2*-KO$^{hep}$-plasma) combined with murine osteogenic differentiation medium to induce osteogenic differentiation. After induction, alkaline phosphatase (ALP) staining and alizarin red staining showed *SIRT2*-KO$^{hep}$-plasma had similar effect on the potential of osteogenic differentiation as LoxP-plasma (Supplementary Fig. 3a). Consistently, the expression of osteogenesis-specific genes Runx2, ALP, SP7, and Osteocalin was not changed in BM-MSCs treated with *SIRT2*-KO$^{hep}$-plasma and LoxP-plasma (Supplementary Fig. 3b), suggesting that hepatocyte SIRT2 had no effect on osteogenic differentiation. Meanwhile, to determine whether the *SIRT2*-KO$^{hep}$-enhanced bone mass is due to decreased bone resorption, we isolated bone marrow-derived monocytes (BMDMs) and induced osteoclast differentiation. BMDMs were cultured with the LoxP-plasma or *SIRT2*-KO$^{hep}$-plasma combined with murine M-CSF and RANKL stimulation for 7 days to generate osteoclasts, subsequently followed by TRAP staining. While LoxP-plasma has potential pro-osteoclastic activity, *SIRT2*-KO$^{hep}$-plasma obviously suppressed osteoclastogenesis, as

157 characterized by the less TRAP-positive osteoclast number with smaller volume (Fig. 2a-c).
158 Moreover, *SIRT2*-KO$^{hep}$-plasma treatment also inhibited the RANKL-induced expression of
159 NFATc1, Acp5, Cathespin K, and DC-stamp, any of which is a critical marker of
160 osteoclastogenesis (Fig. 2d). Altogether, plasma mediates the inhibitory effects of *SIRT2*-KO$^{hep}$
161 on osteoclastogenesis.

162 Next, to explore which components in *SIRT2*-KO$^{hep}$-plasma suppressed
163 osteoclastogenesis, we firstly examined the VitD metabolism in the aged two groups. However,
164 there was no difference in the concentration of plasma total VitD and the expression of hepatic
165 CYP2R1 and CYP27A1 between aged LoxP and *SIRT2*-KO$^{hep}$ group (Supplementary Fig. 4),
166 suggesting the suppression of osteoclastogenesis by *SIRT2*-KO$^{hep}$-plasma is independent of
167 VitD synthesis. To further investigate whether sEVs is required for the protection of *SIRT2*-
168 KO$^{hep}$ against osteoclastogenesis, we isolated sEVs from LoxP-plasma or *SIRT2*-KO$^{hep}$-plasma
169 (LoxP-sEVs or *SIRT2*-KO$^{hep}$-sEVs) and labeled them with PKH26 (a fluorescent lipophilic dye)
170 before co-culturing with BMDMs. Transmission electron microscopy analysis and Western
171 blot confirmed the purity and characteristics of the isolated sEVs (Supplementary Fig. 5a, b).
172 No significant differences in particle shapes and numbers were observed between LoxP-sEVs
173 and *SIRT2*-KO$^{hep}$-sEVs. After 10 hours of co-culture, sEVs may be internalized and mainly
174 found in the cytoplasm in BMDMs (Supplementary Fig. 5c). Importantly, the results showed
175 lower number and smaller volume of TRAP positive osteoclasts from BMDMs treated with
176 *SIRT2*-KO$^{hep}$-sEVs compared with LoxP-sEVs (Fig. 2e-g). However, the *SIRT2*-KO$^{hep}$ plasma
177 had no inhibitive effects on osteoclastogenesis after depletion of sEVs (Fig. 2e-g). Consistently,

the real-time PCR analysis also confirmed that osteoclast-specific genes were down-regulated by *SIRT2*-KO$^{hep}$-sEVs (Fig. 2h).

To further verify whether sEVs directly derived from hepatocytes, not indirectly from other types of cells in liver, regulate osteoclast differentiation, we created a *SIRT2* knockdown cell line in AML12 murine hepatocytes and assessed the effect of their sEVs on osteoclastogenesis. The shape, size, proteins and internalization of sEVs derived from the supernatant of AML12 hepatocytes were similar with those of plasma-derived sEVs (Supplementary Fig. 6). Furthermore, sEVs derived from the medium of SIRT2-knockdown AML12 hepatocytes (sh*SIRT2*-sEVs) markedly reduced osteoclast number, size and expression of osteoclast-specific genes compared with sEVs derived from control AML12 hepatocytes (NC-sEVs) treatment (Fig. 2i-l). In sum, these data provide compelling evidences that SIRT2$^{-/-}$ hepatocytes inhibit osteoclastogenesis through sEVs pathway, suggesting the potential involvement of sEVs in inter-organ crosstalk between liver and bone in osteoporosis.

**SIRT2$^{-/-}$ hepatocyte-derived sEVs contain higher level of LRG1 protein via increasing acetylation of H4K16.** Given that sEVs can transmit molecular cargos into recipient cells, we presumed that SIRT2$^{-/-}$ hepatocyte-sEVs might deliver certain proteins to BMDMs to inhibit its differentiation to osteoclasts. To address this hypothesis, we undertook a global comparison of the plasma proteins of aged LoxP and *SIRT2*-KO$^{hep}$ mice by mass spectrometry, together with mRNA expression profile in the livers by RNA sequencing (RNA-seq) analysis (Fig. 3a and Supplementary Fig. 7a). Among the nine shared regulated proteins, leucine rich alpha-2-glycoprotein 1 (LRG1) expression in the liver and plasma was significantly increased in *SIRT2*-

200 $KO^{hep}$ mice (Fig. 3a). Real-time PCR and Western blot analysis confirmed this observation
201 (Fig. 3b, c). LRG1, a secreted glycoprotein, is a highly conserved member of the leucine-rich
202 repeat family of proteins, many of which are involved in protein-protein interactions and
203 signaling[21]. Western blot analyses showed the vast majority of LRG1 protein in plasma was
204 located in sEVs (Supplementary Fig. 7b). Furthermore, the level of LRG1 protein in the *SIRT2*-
205 $KO^{hep}$-sEVs was higher than that in LoxP-sEVs (Fig. 3c). Consistent with *in vivo* results, *SIRT2*
206 knockdown obviously enhanced LRG1 protein expression both in the cytoplasm and medium-
207 derived sEVs of AML12 hepatocytes (Fig. 3d).

208 It has been previously reported that SIRT2 has a strong preference for acetylation of
209 histone 4 lysine 16 (H4K16ac) in its deacetylation activity[22] (Supplementary Fig. 7c). H4K16ac
210 activates gene transcription by influencing both chromatin structure and interplay with
211 nonhistone proteins[22]. To explore whether SIRT2 regulates LRG1 transcription via
212 deacetylating H4K16ac, we analyzed the previously reported chromatin immunoprecipitation-
213 seq (ChIP-seq) data[23] and predicted three regions in LRG1 promoter containing high
214 acetylation levels on H4K16 (Fig. 3e). Three primers (p1, p2 and p3) encompassing all the
215 regions were designed and the following ChIP result revealed significant higher enrichment of
216 H4K16ac in the three regions in sh*SIRT2*-AML12 hepatocytes compared with control
217 hepatocytes (NC) (Fig. 3f), while no obvious changes were detected in the distant upstream or
218 downstream sites (Supplementary Fig. 7d). The results indicated that SIRT2 inhibits sEVs-
219 LRG1 protein expression through deacetylation of H4K16 in hepatocyte.

220

***SIRT2*-KO$^{hep}$ prevents against OVX-induced bone loss by up-regulating hepatic LRG1 expression.** Since estrogen deficiency increases osteoclast formation, we performed ovariectomy (OVX) in female mice simulating the estrogen loss in postmenopausal women (Fig. 3g and Supplementary Fig. 8a). To find out whether up-regulation hepatic LRG1 is the underlying mechanism for the protective effect of *SIRT2*-KO$^{hep}$ in osteoclastogenesis, LoxP and *SIRT2*-KO$^{hep}$ mice were given injections of either a recombinant adeno-associated viral vector serotype 8 (AAV8) expressing sh*LRG1* under the control of the hepatocyte-specific thyroxin-binding globulin (TBG) promoter (AAV8-sh*LRG1*) or control vector AAV8-NC (Ctrl) (Supplementary Fig. 8b). The AAV8 vector contained a luciferase reporter gene for real-time observation of gene expression by bioluminescence imaging (BLI). The mice were treated with $2\times10^{11}$ viral particles via tail-vein injection 7 days before OVX to maximize the viral expression and knockdown efficiency (Supplementary Fig. 8b). In accordance with the BLI results (Supplementary Fig. 8b), western blot analysis confirmed the knockdown of LRG1 both in hepatocyte and plasma-sEVs in the AAV8-sh*LRG1* group (Supplementary Fig. 8c). As revealed by micro-CT and plasma CTX-1, hepatocyte-specific SIRT2 deficiency prevented against OVX-induced osteoclastogenesis, bone loss (lower BV/TV) and poorly organized trabecular architecture (lower Tb.N. and higher Tb.Sp) (Fig. 3h-j). Moreover, the knockdown of hepatocyte LRG1 completely reversed the osteoclastogenesis and bone phenotype in *SIRT2*-KO$^{hep}$-OVX mice group (Fig. 3h-j). All these results indicate that the alleviated bone loss and osteoporosis in *SIRT2*-KO$^{hep}$-OVX mice is, to a large extent, a consequence of up-regulating LRG1 expression in hepatocytes.

**LRG1 is the cargo of hepatocyte-derived sEVs to mediate the protection of *SIRT2*-KO$^{hep}$ against osteoclastogenesis and bone loss.** We continued to verify the connection between LRG1 in sEVs (sEVs-LRG1) and the protective role of *SIRT2*-KO$^{hep}$ in osteoporosis. The sEVs were purified from the supernatant of sh*SIRT2*-AML12 cells infected with an empty vector (Ctrl) or sh*LRG1* lentiviral vectors. And then BMDMs were co-cultured with each set of transduced sEVs and murine M-CSF/RANKL stimulation for 7 days to generate osteoclasts (Fig. 4a). Compared with *SIRT2*-knockdown AML12 cells-derived sEVs (sh*SIRT2*-sEVs), *SIRT2* and *LRG1* double-knockdown AML12 cells-derived sEVs (sh*SIRT2*-sh*LRG1*-sEVs) resulted in enhanced osteoclastogenesis, as indicated by the greater number and size of TRAP positive osteoclasts from BMDMs (Fig. 4b-d) and the increased expression of osteoclast-specific genes (Fig. 4e). These data suggest SIRT2-regulated sEVs-LRG1 is directly linked to osteoclastogenesis. To further verify the mechanism and the therapeutic potential of sEVs-LRG1 in osteoporosis *in vivo*, we consecutively intravenously injected the mice with the control-sEVs (NC-sEVs), sh*SIRT2*-sEVs and sh*SIRT2*-sh*LRG1*-sEVs (50μg per mouse, every other day) 3 days after OVX (Fig. 4f). Biophotonic imaging detected the intraosseous fluorescence signal in mice administrated with PKH26-labeled sEVs at either 4 or 8h after administration (Fig. 4g) as previously described[24]. Six weeks after the first injection, micro-CT and the TRAP staining showed that sh*SIRT2*-sEVs significantly abolished OVX-induced bone loss, poor organized trabecular architecture (Fig. 4h, i) and osteoclastogenesis (Fig. 4j-l). However, sh*SIRT2*-sh*LRG1*-sEVs reversed the osteoclastogenesis and bone phenotype in sh*SIRT2*-sEVs-treated OVX mice (Fig. 4h-l), indicating sEVs-LRG1 is required for the protection of sh*SIRT2*-sEVs against bone loss *in vivo*. Thereafter, we investigated the

265 therapeutic potential of sEVs-LRG1 in osteoporosis. Impressively, the present results showed
266 substantially higher trabecular bone mass and better trabecular architecture as well as less
267 TRAP-positive osteoclasts and lower osteoclast activities in the OVX mice treated with sEVs
268 derived from *LRG1*-overexpressed AML12 cells (LRG1-sEVs) when compared with those in
269 NC-sEVs-treated OVX mice (Fig. 4h-l). Of note, the therapeutic effect of LRG1-sEVs was
270 even better than sh*SIRT2*-sEVs. Together, these data demonstrate that LRG1 is the bona fide
271 functional cargo of hepatocyte-drived sEVs mediated the therapeutic effect of *SIRT2*-KO$^{hep}$ on
272 osteoclastogenesis and bone loss.

273

274 **Hepatocyte-derived sEVs-LRG1 suppresses osteoclast differentiation by inhibiting**
275 **RANKL-induced NF-κB p65 nuclear translocation.** To understand the mechanism
276 underlying the inhibitive effect of hepatocyte-derived sEVs-LRG1 on osteoclastogenesis, we
277 isolated sEVs from the medium of AML12 hepatocytes transduced with LRG1-GFP fusion
278 protein and then observed the sEVs-LRG1-GFP internalization. Immunostaining analysis
279 showed that after either 12h or 24h of co-culture, most of hepatocyte-derived sEVs were
280 internalized and LRG1-GFP, co-localized with PKH26, evenly distributed in the cytoplasm of
281 BMDMs (Supplementary Fig. 9a). Given that hepatocyte-derived sEVs can transmit molecular
282 cargos into recipient cells and LRG1 mediates protein-protein interactions as reported
283 previously, the screening of proteins interacting with hepatocyte-derived sEVs-LRG1 was
284 performed in BMDMs. We treated the BMDMs with the sEVs derived from the AML12 cells
285 overexpressed Flag-LRG1 (Flag-LRG1-sEVs), followed by affinity purification using an anti-
286 Flag antibody, and the bound proteins were analyzed by liquid chromatography with tandem

mass spectrometry (LC-MS/MS). MS analysis revealed that nuclear factor kappa B (NF-κB) p65 was the only predicted pro-osteoclastic factor among the proteins interacting with sEVs-LRG1 (Fig. 5a and Supplementary Fig. 9b). Further, both IP assay and immunofluorescence staining validated the endogenous interaction of sEVs-LRG1 with p65 in the cytoplasm of primary BMDMs (Fig. 5b, d). More importantly, LRG1-sEVs obviously abolished RANKL-induced p65 phosphorylation (Fig. 5c) and nuclear translocation (Fig. 5d) in primary BMDMs.

LRG1 is previously reported to promote angiogenesis by modulating endothelial TGF-β signaling[21]. The immunohistochemistry (IHC) data showed a similar amount blood vessel in distal femur of aged *SIRT2*-KO$^{hep}$ mice compared with that of aged LoxP mice (Supplementary Fig. 9c, d). Meanwhile, MS results showed no component of TGF-β receptor complex binding to sEVs-LRG1, and Western blot revealed that LRG1-sEVs had no effect on the RANKL-induced TGF-β signaling activation in primary BMDMs, including Smad1/5 and Smad2/3 signaling (Fig. 5c). These data exclude the possibility that the inhibition of osteoclastogenesis by sEVs-LRG1 was due to promoting TGF-β signaling and angiogenesis. Next, we wanted to determine whether the nuclear translocation of p65 is necessary for the suppression of sEVs-LRG1 in osteoclast differentiation. Neither Sc-3060 nor JSH-23, the inhibitors of p65 nuclear translocation, can further inhibit RANKL-induced NFATc1 signaling activation in the osteoclasts administrated with LRG1-sEVs (Fig. 5f), as well as the number and size of osteoclast (Fig. 5e). In contrast, p65 overexpression totally reversed the sEVs-LRG1-induced inhibition of osteoclastogenesis and NFATc1 signaling in RANKL-treated RAW264.7 cells (Fig. 5g, h and Supplementary Fig. 9e). In sum, these data support the mechanism that

hepatocyte-derived sEVs-LRG1 suppresses osteoclast differentiation through negatively regulating NF-κB-NFATc1 signal pathway.

**Pharmacological inhibition of SIRT2 attenuates bone loss and osteoporosis.** Given the protective role of *SIRT2*-KO$^{hep}$ in both age-related and OVX-induced osteoporosis, we evaluated whether AGK2, a specific SIRT2 inhibitor, can be repositioned for prevention or treatment of osteoporosis. As expected, six-week intraperitoneal injection of AGK2 (50mg/kg, every other day, started 3 days after OVX) markedly up-regulated the LRG1 protein level both in the livers and plasma-sEVs of the OVX-C57BL/6 mice (Fig. 6a, b). Notably, AGK2 treatment significantly increased bone mass and improved trabecular architecture in OVX mice (Fig. 6c, d). The intraperitoneal injection of AGK2 may be widely distributed throughout the body. Therefore, we asked whether intraperitoneal AGK2 treatment worked mainly through inhibiting SIRT2 in hepatocytes, not in other types of cells. To do so, we evaluated the efficiency of AGK2 in *SIRT2*-KO$^{hep}$ mice. Notably, there is no difference in bone mass and trabecular architecture between vehicle-treated and AGK2-treated OVX-*SIRT2*-KO$^{hep}$ mice (Fig. 6e, f), suggesting hepatocyte SIRT2 is the major therapeutic target of AGK2. Thus, pharmacological inhibition of SIRT2 is a promising approach that should be effective for the prevention and treatment of osteoporosis.

**Hepatocyte-derived sEVs-LRG1 inhibit human osteoclast differentiation.** In our final analyses, we investigated whether SIRT2 inhibition and sEVs-LRG1 could also suppress

human osteoclast differentiation. For this purpose, we isolated primary human peripheral blood mononuclear cells (PBMCs) and induced osteoclast differentiation according to the previous report[25]. PBMCs were cultured with the sEVs purified from the supernatant of human hepatocyte HepG2 cells stably transfected with sh*SIRT2* (sh*SIRT2*-HepG2-sEVs) or control (NC-HepG2-sEVs) plasmids. Western blot confirmed the knockdown of SIRT2 in sh*SIRT2*-hepatocytes and the up-regulation of LRG1 protein in sh*SIRT2*-HepG2-sEVs (Fig. 7a). Similar to the finding in mice, sh*SIRT2*-HepG2-sEVs treatment obviously inhibited osteoclasts differentiated from PBMCs (Fig. 7b-d). Similarly, the supplementing with human sEVs derived from HepG2 cells treated with AGK2 (AGK2-HepG2-sEVs) obviously abolished RANKL-induced differentiation of human PBMCs (Supplementary Fig. 10). Further, sEVs were isolated from the patients' plasma. The sEVs-LRG1 were measured by Western blot and the expression of sEVs-LRG1 from a 65-year-old patient without osteoporosis or other metabolic disease served as a control. The present results showed that sEVs with LRG1 high expression ($LRG1^{high}$ plasma-sEVs) resulted in less number and size of TRAP positive osteoclasts differentiated from PBMCs as compared with the treatment of sEVs drived from LRG1 low expressed human plasma ($LRG1^{low}$ plasma-sEVs) (Fig. 7e-h), as well as the decreased expression of osteoclast-specific genes (Fig. 7i). In sum, hepatocyte-derived LRG1-rich sEVs significantly suppress RANKL-induced human osteoclast differentiation.

**Plasma-sEVs-LRG1 positively correlates with BMD and inversely correlates with bone resorption marker in patients.** To gain insights into human disease, we analyzed data from 120 patients with osteoporosis or normal bone mass for associations between bone-related

parameters and plasma sEVs-LRG1 levels. The patients presented different protein level of plasma-sEVs-LRG1 and bone mineral density (BMD), the golden standard in the diagnosis of osteoporosis assessed using dual X-ray absorptiometry (DXA). Importantly, compared with normal female control group (normal bone density), there was significantly decreased protein level of plasma-sEVs-LRG1 in the female osteoporotic patients by Western blot (Fig. 7j, k). Moreover, plasma-sEVs-LRG1 protein expression was strongly and positively correlated with BMD and inversely related to the clinical bone resorption marker β-CTX (Fig. 7l, m). In comparison, there was no association between plasma-sEVs-LRG1 level and the clinical bone formation marker PINP and bone-specific alkaline phosphatase (BALP) (Fig. 7n, o). Collectively, our results suggest that plasma-sEVs-LRG1 suppresses clinical bone resorption.

## Discussion

The current study describes a novel and highly significant function of hepatocyte-osteoclast communication mediated by sEVs using patient specimens, along with animal and cell models. Our results show that hepatocyte-specific *SIRT2* deficiency (*SIRT2*-KO$^{hep}$) obviously abolishes bone loss in aged and postmenopausal osteoporosis mouse models. Mechanistically, we revealed for the first time that *SIRT2*-KO$^{hep}$-upregulated hepatic LRG1 transfers to BMDMs through hepatocyte-derived sEVs, resulting in inhibition of NF-κB p65-NFATc1 activation and osteoclastogenesis. Our findings greatly extend our current understanding of the pathophysiological role of liver in bone metabolism and suggest the liver-bone communication by SIRT2-sEVs-LRG1 may function to restore bone homeostasis in old people or postmenopausal women. Importantly, treatment with AGK2 or LRG1-sEVs conferred a

therapeutic benefit in osteoporosis, including animal models and human primary cell culture, corroborating targeting hepatocyte SIRT2 or sEVs-LRG1 as a promising therapeutic modality in primary osteoporosis.

SIRT2 has been implicated in the aging process and liver diseases. Our group recently found that hepatic SIRT2 prevents ALD through deacetylating CCAAT/enhancer-binding protein beta (C/EBPβ)[20]. In addition, we also reported that SIRT2 in macrophage prevents and reverses aging-associated inflammation and insulin resistance through deacetylation of NLRP3[19]. For bone metabolism, Jing et al reported that SIRT2 deficiency in BMDMs prevents age-related bone loss in rats by inhibiting osteoclastogenesis[26]. As the whole body SIRT2 knockout rats were used, the study did not allow for consideration of potential interaction among different organs and there is the possibility that hepatocyte SIRT2 deficiency contribute to the protective effects on bone loss. Whether SIRT2 in BMDMs play roles in the osteoporosis in vivo remains to be explored using the real physiological aged BMDM-specific SIRT2 knockout animal model. In the present study, we mainly focused on the function of hepatic SIRT2 in osteoporosis, therefore the liver-specific knockout mice and AAV8 viral expression system with hepatocyte-specific TBG promoter were used to exclude the influence of SIRT2 in other organs. Notably, AGK2 treatment cannot further improve the ameliorated bone mass and trabecular architecture in OVX *SIRT2*-KO$^{hep}$ mice, suggesting hepatocyte SIRT2 is the primary factors for the protective role of whole body SIRT2 knockout in osteoporosis. Moreover, hepatic SIRT2 exert its effect on osteoclast differentiation mainly through up-regulating the sEVs cargo LRG1 protein level, not affecting sEVs biogenesis, maturation, and secretion.

There are many hepatic non-sEVs-related hormonal and signaling effectors involved in bone metabolism besides sEVs. We have ruled out the previously reported non-sEV-related hormonal and signaling effectors in this novel SIRT2-regulated live-bone axis. Firstly, we tested VitD metabolism and find there was no difference in the concentration of plasma total VitD and the expression of hepatic CYP2R1 and CYP27A1 between aged LoxP and *SIRT2*-KO$^{hep}$ group (Supplementary Fig. 4). Secondly, the hepatic effectors mediated liver-bone axis were mainly transferred to bone cells via blood. We carefully checked the original MS data and found there was no difference in the concentrations of the hormonal or signaling effectors involved in liver-bone axis previously reported between the two groups, including fibroblast growth factor 21 (FGF21), insulin-like growth factor binding protein 1 (IGFBP1)[13,27], lecithin-cholesterol acyltransferase (LCAT)[28], transforming growth factor-β (TGF-β)[12,29,30] and insulin-like growth factor 1 (IGF-1)[31-33]. Though MS data showed the higher level of fibronectin in *SIRT2*-KO$^{hep}$ mice, the result does not match our phenotype according to the previous report that fibronectin inhibits osteoblast function[34,35]. Thirdly, previous reports showed that alterations in plasma cholesterol and bilirubin were involved in the regulation of osteoblast and osteoclast activities[28,34,36]. No significant differences in the concentrations of the plasma cholesterol and bilirubin were observed between aged LoxP and *SIRT2*-KO$^{hep}$ mice (data not shown). Furthermore, the *SIRT2*-KO$^{hep}$ plasma had inhibitive effects on osteoclastogenesis, but the inhibitive effects were abolished after depletion of sEVs (shown in Fig. 2e-g). All of these results suggested that SIRT2$^{-/-}$ hepatocyte-derived sEVs, not non-sEV-related hormonal and signaling effectors, abolish osteoclastogenesis.

This study provides the first evidence to our knowledge that hepatocyte-derived sEVs

417 directly transfer anti-resorption factors from liver to intraosseous osteoclasts. Moreover, LRG1
418 in hepatocyte-derived sEVs was originally discovered as an osteoclasts cell fate determinant.
419 LRG1 is expressed abundantly in hepatocytes, but lowly in osteoclasts. Our results showed that
420 the vast majority of secreted LRG1 protein in aged plasma located in sEVs (Supplementary
421 Fig. 7b), explaining why the *SIRT2*-KO$^{hep}$ plasma has no inhibitive effects on
422 osteoclastogenesis after depletion of sEVs (Fig. 2e-g). LRG1 is previously reported to promote
423 angiogenesis by tipping the balance of TGFβ1 signaling toward the ALK1/Smad1,5,8 pathway
424 in endothelial cells (EC), which is dependent on the presence of the TGFβ1 type III receptor,
425 endoglin[21]. However, we firstly demonstrated here that hepatocyte-derived sEVs-LRG1 exerts
426 its function in osteoclasts through a novel mechanism independent of the receptor endoglin.
427 The MS and Western Blot results showed no interaction between sEVs-LRG1 and endoglin
428 and no activation of TGFβ1 signaling. The immunofluorescence showed no binding of LRG1
429 on cell membrane and strong signal in cytoplasm. Furthermore, hepatocyte-derived sEVs-
430 LRG1 directly binds to p65 and inhibits p65 nuclear translocation after uptake by BMDMs. It
431 has been widely reported that phosphorylation of p65 results the nuclear translocation[37-41],
432 whether sEVs-LRG1 directly binds to the phosphorylation site of p65 or whether sEVs-LRG1
433 affects the binding of other phosphorylases to p65 needs further study. Therefore, here we
434 revealed a direct inter-organ regulatory mode between histone acetylation in hepatocytes and
435 phosphorylation of transcription factor in osteoclasts via sEVs protein cargo transfer. While
436 intracellular NF-κB p65-NFATc1 signal is over-activated in osteoclasts, LRG1 protein
437 transferred into osteoclasts by the extracellular hepatocyte-derived sEVs act as a brake on pro-
438 osteoclastic activity to maintain bone homeostasis (Fig. 5).

Osteoporosis is one of the major health problems worldwide and its incidence is growing with the aging population[42,43]. Moreover, accumulating studies reported that osteoporosis is a frequently observed complication in patients with CLD, particularly liver cirrhosis and cholestatic liver diseases[12,44]. The elusive mechanisms and poor outcomes are getting more and more attention. Therefore, identification of novel therapeutic targets on liver-bone communications is an urgent clinical need in primary osteoporosis. Epigenetics studies have provided new understandings in the mechanism of treatment and pathophysiology of bone remodeling occurring in osteoporosis. SIRT1 and SIRT6 have been implicated in bone metabolism[45,46]. A randomized, double-blind, placebo-controlled trial investigated the effects of resveratrol, an agonist of SIRT1, on BMD in obese subjects. Results indicated a significant dose-dependent increase of bone alkaline phosphatase and bone mineral density, but to date, no data have been reported for osteoporotic women[47]. In the present study, the specific inhibitor of SIRT2, AGK2 was verified as a promising therapeutic agent for osteoporosis in OVX mice through mainly targeting hepatocyte SIRT2, not osteoclast SIRT2. In the past few years, extracellular vesicles-based engineered delivery systems for precision nanomedicine have attracted wide interest across areas of molecular cell biology, pharmaceutical sciences, and nanoengineering[48]. Here, we also identified LRG1-rich sEVs as an effective therapy for treatment of osteoporosis in mice. Moreover, sEVs derived from either human LRG1$^{high}$ plasma or human hepatocytes with SIRT2 inhibition (by AGK2 or shRNA) significantly suppress RANKL-induced osteoclastogenesis. The positive correlation between plasma sEVs-LRG1 expression and BMD in clinical samples further strengthens the therapy potential of LRG1$^{high}$-sEVs. Meanwhile, we analyzed the liver proteomics data of the hepatic osteodystrophy patients

in the recent report[28]. There was the trend that the cirrhosis patients with the decreased expression of hepatic LRG1 have lower bone mass, though the statistical difference was not statistically significant. Here we mainly focused on the primary osteoporosis without liver diseases and the correlation between hepatic LRG1 expression and primary osteoporosis still needs more clinical samples and further study. Therefore, our data provide definitive evidence that targeting hepatic SIRT2 or sEVs-LRG1 is a powerful strategy for primary osteoporosis therapy.

In summary, our findings therefore unveiled a novel working model of liver-bone communication, depicted in Fig.8, to illustrate that hepatocyte SIRT2 regulates pro-osteoclastic signaling of NF-κB p65 in osteoclasts through sEVs-LRG1 pathway. The inter-organ action of SIRT2-sEVs-LRG1-NF-κB-NFATc1 axis may also be essential to maintaining bone homeostasis and a promising therapeutic target in primary osteoporosis.

## Methods

**Animals.** The hepatocyte-specific SIRT2 knockout mice (*SIRT2*-KO$^{hep}$) were produced by crossing SIRT2$^{flox/flox}$ mice obtained from Johan Auwerxd Laboratory (Switzerland) and Alb-Cre mice purchased from Jackson Laboratory (U.S) in a C57BL/6 background.C57BL/6 female mice were purchased from the Shanghai SLAC Laboratory Animal Co. Ltd. All mice were housed at a specific pathogen-free (SPF) environment in the Animal Laboratory Unit of School of Medicine, Shanghai Jiaotong University (Shanghai, China), and all mice were provided with sterile food and water. The animal experiments were performed in accordance with the approved guidelines by the Institutional Animal Care and Use Committee at Shanghai Jiaotong University School of Medicine.

**Micro-CT analysis.** Quantitative tomography of distal femoral metaphysis was performed using an X-ray micro-tomography (Skyscan1076, Bruker micro-CT, Belgium). Region-of-interest (ROI) was defined from 0image slice to 200 image slices, where the growth plate slice was defined as 0 image slice. The standardized region of femura were scanned at 9-μm resolutions. Trabecular bone mass and microarchitecture were defined including trabecular bone volume/tissue volume ratio (BV/TV), trabecular number (Tb.N.), trabecular separation (Tb.Sp) and trabecular thickness (Tb.Th).

**ELISA.** The blood collected from mice was centrifuged for 30 min at 2000 g, and the plasma was harvested and stored at -80℃ for subsequent assays. Type 1 collagen amino-terminal propeptide (P1NP), Type 1 collagen C breakdown products (CTX-1) (Elabscience) and total VitaminD (J&L biological) concentrations in the plasma were all performed according to the manufacturer's instructions.

**Histology and immunohistochemistry.** After routine 4% formaldehyde fixed, decalcification with 10% EDTA (pH 7.4) for 1 week and paraffin embedded (FFPE) specimen processing, bone sections (5-7μm) were stained with hematoxylin and eosin (H&E) and TRAP staining for histological evaluation of osteoblasts and osteoclasts in mice. Osteoclasts and osteoblasts surface were assessed relatively to the total bone surface as Oc.S/BS and Ob.S/BS. The expression levels of $CD31^+$ vessels in the bone tissue slides of aging mice were tested using immunohistochemistry (IHC) according to the standard procedure. The corresponding primary

antibodies (dilution 1:50 for anti-CD31 antibody) and HRP-conjugated secondary antibody were obtained from Servicebio Biotechnology, Inc. The quality control for IHC was administered with controls. Quantification of $CD31^+$ vessels/bone surface ratio were measured.

**Cell culture.** Mouse hepatic cell lines (AML12) were obtained from American Type Culture Collection (ATCC, USA). They were cultured in DMEM/F12 with 10% fetal bovine serum (Sigma), 40ng/ml dexamethasone (Sigma), 1% Liquid Media Supplement (ITS, Sigma) and incubated in a humidified atmosphere at 37℃ and 5% $CO_2$. Human hepatic cell lines (HepG2) were cultured in DMEM with 10% fetal bovine serum (Sigma) and incubated in a humidified atmosphere at 37℃ and 5% CO2. HEK293T cells were maintained in DMEM supplemented with 10% fetal bovine serum (Sigma). Mouse primary bone marrow mesenchymal stem cells (BM-MSCs) were isolated from femur and tibia bones from 2-4 weeks old C57BL/6 mice. Femur and tibia bones were obtained, rinsed while stripping muscle tissue, soft tissue was removed and transferred to the culture medium. Bone tissue was shredded with forceps and the shredded bone was rinsed with a 1 ml syringe to obtain bone marrow cells, which were inoculated and cultured. The culture medium was changed after 2 days and passaged for culture. The cells at passages 6 are used for cell function experiments. Mouse primary bone marrow derived monocytes (BMDMs) were isolated from C57BL/6 femur and tibia bones from 6-8 weeks old. Briefly, the bone marrow cells were flushed out from long bones with α-MEM medium (HyClone). Cell suspensions were filtered through a 100 μm cell strainer (FALCON) and cultured in α-MEM supplement with 10% fetal bovine serum (Sigma), 1% penicillin/streptomycin (Invitrogen) and 1% GlutaMAX™ Supplement (Thermo Fisher). After 24 hours, the supernatant was collected and cell precipitation was obtained by centrifugation, then BMDMs were attached in a-MEM medium supplemented with 10% FBS, 1% GlutaMAX™ Supplement and 30 ng/ml murine macrophage colony-stimulating factor (M-CSF) (Peprotech), BMDMs were harvested at day 2 after M-CSF stimuli. For osteogenic induction, BM-MSCs were seeded in 12-well plates and treated with osteogenic medium (Cyagen). The culture medium was replaced every other day. 7-14 days later, Osteogenic differentiation was assessed by ALP staining (Beyotime Biotechnology) and alizarin red staining (Cyagen) according to manufacturer's protocol, respectively. For osteoclast differentiation, harvested BMDMs were scraped and seeded into 12-well plates at a

concentration of $1\times10^5$ cells per well for differentiation experiments. Cells were stimulated with 50ng/ml receptor activator of nuclear factor-kappa B ligand (RANKL) (R&D, 462-TEC-010) and 30 ng/ml M-CSF (Peprotech, 315-02-50) for 7 days, and the medium was replaced every 2 days. Osteoclasts were fixed and stained using the TRAP staining kit (Sigma-Aldrich, 387A-1KT).

**sEVs isolation and identification.** The mouse hepatic AML-12 cell lines were cultured in the normal medium until 60%-70% confluency; and then the medium was replaced with10% sEVs-depleted FBS and cultured in normal conditions for 2 days. Then, the medium was harvested and centrifuged at 300g for 10 minutes, 2,000g for 10 minutes, 10,000g for 30 minutes, and then ultracentrifuged at 110,000g for 90 minutes (Beckman Ultra high speed refrigerated centrifuge, CA, USA), and the sediment was resuspended with PBS and stored at -80℃ for further use. After the plasma is diluted with PBS, ultracentrifugation is performed to obtain sEVs in plasma. The concentration of the sEVs was detected by the Bicinchoninic Acid (BCA) Protein Assay Kit. The size of sEVs was analyzed using the Electrophoresis & Brownian Motion Video Analysis Laser Scattering Microscopy. Besides, the microscopic image of sEVs were observed by transmission electron microscopy. Moreover, protein markers of sEVs, including Alix, HSP70 and TSG101 were measured by western blot analysis.

**Exosomes labeling and tracking.** Purified sEVs isolated from plasma or culture medium were collected and labeled with PKH26, a red fluorescent membrane dye (Sigma) according to the manufacturer's instructions. Then, the labeled sEVs were isolated with Exoquick Reagent (SBI, USA), briefly, the labeled sEVs were incubated with Exoquick reagent (5:1) for overnight, and centrifuged at 1,500g for 30 minutes, then the sEVs were resuspended in PBS and added to the BMDMs for sEVs uptake studies. After incubation for hours at 37℃, cells were observed by Laser scanning confocal microscope (Nikon, Japan).

**RNA interference.** For construction of stable cell lines, the shRNAs cloned into the pGIPZ vector were obtained from scientific research platform of Shanghai Jiao Tong University School of Medicine (SJTU-SM) (Shanghai, China).

The cDNA target sequences of shRNAs, and primer sequences used for cloning in this study.

| Name | Species | Sequence (5'->3') |
|---|---|---|
| The cDNA target sequences of shRNAs | | |
| shSIRT2-1 | Mouse | CCAACCATCTGCCACTACT |
| shSIRT2-2 | Mouse | AGCTGTTGGTGGATGAGCA |
| shLRG1 | Mouse | GGCCTACAGCACCTGGATA |
| shSIRT2-1 | Human | TGGACGAGCTGACCTTGGA |
| shSIRT2-2 | Human | AGCGCGTTTCTTCTCCTGT |
| Primers sequences used for cloning | | |
| LRG1 | Mouse | Forward: ATGGTCTCTTGGCAGCATCA Reverse: TTACTTATCGTCGTCATCCT |

HEK293T cells were co-transfected with the lentivirus vector described above and packaging vectors psPAX2 and pMD2.G with Lipofectamine 2000 transfection reagent (Invitrogen) for producing lentivirus. The p65 plasmids were transfected into raw264.7 cells with Lipofectamine3000 transfection reagent (Invitrogen) according to the manufacturer's instruction.

**Western blot analysis.** Cells, mouse tissue or sEVs were lysed in SDS-lysis buffer. The protein samples were loaded into the SDS-PAGE gels and then transferred onto 0.45um or 0.22um nitrocellulose membranes (Axygen, USA). Membranes were blocked with 5% skimmed milk at room temperature for 1h and incubated with primary antibodies at 4℃ for overnight, following by incubation with the HRP-conjugated secondary antibodies at room temperature for 1h. Finally, the membranes were visualized with an Enhanced Chemiluminescence (ECL) Detection Kit (Millipore, USA) and by using Image Quant LAS 4000 Mini (GE Healthcare Bio-Sciences AB, Uppsala, Sweden). The primary antibodies used in the experiments were anti-TSG101 (1:1000; Proteintech), anti-HSP70 (1:1000; Proteintech), anti-Alix (1:1000; Proteintech), anti-β-actin (1:5000; Cell Signaling Technology). anti-SIRT2 (1:500; Sigma), anti-LRG1 (1:500; Proteintech), anti- β -tubulin (1:2000; Proteintech), anti-rabbit IgG (1:5000; Cell Signaling Technology), anti-FLAG (1:2500; Sigma), anti-mouse IgG (1:5000; Cell

Signaling Technology). anti-p-p65 (1:1000; Cell Signaling Technology), anti-p65 (1:1000; Cell Signaling Technology), anti-p-Smad2/3 (1:500; Cell Signaling Technology), anti-T-Smad2/3 (1:1000; Cell Signaling Technology), anti-p-Smad1/5 (1:500; Cell Signaling Technology), anti-T-Smad1 (1:1000; Cell Signaling Technology), anti-T-Smad5 (1:1000; Cell Signaling Technology).

**Quantitative RT-PCR.** Total RNA was extracted from cells or mouse tissue by Trizol reagent (Invitrogen) and was reverse-transcribed into cDNA with AMV Reverse Transcriptase XL (Takara, Japan). Quantitative real-time PCR was performed using SYBR Green PCR Master Mix (Applied Biosystems) and on the ABI 7300 PCR system (Applied Biosystems). The primer sequences used were as follows:

Primers sequences used for real-time PCR.

| Name | Species | Sequence (5'->3') |
|---|---|---|
| RPL13A | Mouse | Forward: GAGGTCGGGTGGAAGTACCA |
| | | Reverse: TGCATCTTGGCCTTTTCCTT |
| LRG1 | Mouse | Forward: CCATGTCAGTGTGCAGATTC |
| | | Reverse: AAGAGTGAGAGGTGGAAGAG |
| Runx2 | Mouse | Forward: GCATGGTGGAGGTACTAGCTG |
| | | Reverse: GCCGTCCACTGTGATTTTG |
| Sp7 | Mouse | Forward: ATGGCGTCCTCTCTGCTTG |
| | | Reverse: TGAAAGGTCAGCGTATGGCTT |
| ALP | Mouse | Forward: ATCTTTGGTCTGGCTCCCATG |
| | | Reverse: TTTCCCGTTCACCGTCCAC |
| Osteocalcin | Mouse | Forward: GCAATAAGGTAGTGAACAGACTCC |
| | | Reverse: GTTTGTAGGCGGTCTTCAAGC |
| GAPDH | Mouse | Forward: ACTGAGGACCAGGTTGTC |
| | | Reverse: TGCTGTAGCCGTATTCATTG |
| NFATc1 | Mouse | Forward: GGAGAGTCCGAGAATCGAGAT |
| | | Reverse: TTGCAGCTAGGAAGTACGTCT |
| Cathespin K | Mouse | Forward: GGAGTTGACTTCCGCAATCCT |

| | | |
|---|---|---|
| | | Reverse: ACTTGAACACCCACATCCTGC |
| Acp5 | Mouse | Forward: AGCAGCTCCCTAGAAGATGGA |
| | | Reverse: AGCCACAAATCTCAGGGTGG |
| DC-STAMP | Mouse | Forward: CCGTGAAGGTAGGAACGCTT |
| | | Reverse: AGATTCAGCGGAGTGGCAAG |
| CYP2R1 | Mouse | Forward: TCAACTGTCGTTCTAAATGGCT |
| | | Reverse: TCTGGAATTGAGTAAGCCTCCC |
| CYP27A1 | Mouse | Forward: TCCAGGCACAGGAGAGTACG |
| | | Reverse: TACTTGGTCTTGTTCAGCACCTGG |
| NFATc1 | Human | Forward: CCAGTCCCTTCCAAGTTTCCA |
| | | Reverse: GCATAGCCATAGTGTTCTTCCT |
| CTSK | Human | Forward: TTCCCGCAGTAATGACACCC |
| | | Reverse: GGAACCACACTGACCCTGAT |
| ITGB3 | Human | Forward: TGGTAGAAGAGCCAGAGTGTC |
| | | Reverse: TACAGTGGGTTGTTGGCTGT |
| CALCR | Human | Forward: CCCCAGGATGCAATTTTCTGG |
| | | Reverse: AGAATTGGGGTTGGGTGATTTAG |
| GAPDH | Human | Forward: TCGGAGTCAACGGATTTGGT |
| | | Reverse: TTCCCGTTCTCAGCCTTGAC |

**RNA-seq and LC-MS/MS.** RNA from liver tissus (20mg) was extracted. Total RNA was processed with mRNA enrichment method or rRNA removal method. Oli god T magnetic beads were used to enrich the mRNA with poly A tail; DNA probe were used to hybridize rRNA and RNase H were used to selectively digest the DNA/RNA hybrid chain, and then digest the DNA probe with DNase I. After purification, the obtained RNA was fragmented with the interrupted buffer. Then First-strand cDNA was generated using reverse transcription with random N6 primers, followed by two-strands cDNA synthesis to form double-stranded DNA. Afterwards, fill up the synthetic double-stranded DNA ends and phosphorylate the 5'end, and form a sticky end protruding an "A" at the 3'end, and then connect a blister linker with a protruding "T" at the 3'end. The ligation product is amplified by PCR with specific primers. The PCR product is

heat-denatured into single-stranded, and then the single-stranded DNA is circularized with a bridge primer to obtain a single-stranded circular DNA library. Sequencing using the DNBSEQ platform (BGI-Shenzhen, China).

Differentially expressed proteins in the plasma of aged LoxP and *SIRT2*-KO$^{hep}$ mice were determined by mass spectrometer of the Basic Medicine Public Technology Platform of SJTU-SM.

**Chromatin Immunoprecipitation.** Enrichment of H4K16ac on LRG1 promoter region from H4K16ac CHIP-seq is predicted in Cistrome Data Browser. ChIP analysis was performed using the Millipore ChIP Assay Kit (Millipore, MA, USA) according to the manufacturer's instructions. Briefly, ChIP was performed with $5\times10^6$ cells per reaction. Cells were crosslinked with formaldehyde for 10 min at room temperature and then sonicated. Corresponding IgG was used as controls. The precipitated DNA was quantified by qRT-PCR.

Primers sequences used for CHIP are as follows.

| Name | Species | Sequence (5'->3') |
|---|---|---|
| LRG1-chip-primer1 | Mouse | Forward: CAGACCTGGCACCAAGCTAA |
| | | Reverse: GCAGGCCTGAATCTGTTCCT |
| LRG1-chip-primer2 | Mouse | Forward: ACACTGTCCATCTGTCGGTG |
| | | Reverse: GAGAGCATTGCGGGTCAGAT |
| LRG1-chip-primer3 | Mouse | Forward: TAACTCTCTGTCCAGCACGC |
| | | Reverse: TTGTGGGAGATGTCGAAGCC |
| LRG1-chip-primer4 | Mouse | Forward: CGCCAACCGAAACAAGATGT |
| | | Reverse: TGACATGGGACCACATTGGC |
| LRG1-chip-primer5 | Mouse | Forward: GGGCCTACAGCACCTGGATA |
| | | Reverse: GAGATGTCGAAGCCGTCCTG |

**Adeno-associated Virus 8 (AAV8)-mediated gene expression.** An AAV8 delivery system was used to specifically knock down murine LRG1 in mouse liver. The open reading frame encoding LRG1 gene, without a stop codon, was cloned into an AAV8 package vector pAAV-TBG-T2A-luciferase. The mice were injected $2\times10^{11}$viral particles of AAV8 containing either

target gene or scrambled vector via the tail vein 7 days before OVX model construction. The target gene expression was monitored by Bioluminescence imaging (BLI) through intraperitoneal injection of D-luciferin (150μg/g BW).

**Ovariectomy (OVX) mouse model.** For studies in vivo, mice were randomly divided with weight. For the ovariectomy-induced bone loss model, sham-opreation or ovariectomy were performed in 12-16 weeks old female mice. After weeks of treatment, femurs were isolated for micro-CT or histology analysis, blood was collected for CTX-1 test.

**Nano-LC-ESI-MS/MS analysis.** Nano-LC-MS/MS with electrospray ionization (the Basic Medicine Public Technology Platform of SJTU-SM) (Shanghai, China) was used to identify interacting proteins. In brief, sEVs contained FLAG-LRG1 protein (sEVs-FLAG-LRG1) were purified from culture medium of AML12 cells stably transfected Flag-tagged LRG1 expression. After co-cultured with sEVs-FLAG-LRG1 for 48h, BMDMs were harvested, lysed, and briefly sonicated at 4°C. The supernatants (whole-cell lysates) were collected and incubated with Protein A/G PLUS-Agarose (Santa Cruz, sc-2003) at room temperature for 1h, and then mixed protein lysates were subjected to immunoprecipitation with anti-FLAG M2 beads (Sigma). Immunoprecipitation samples were separated by SDS-polyacrylamide gel electrophoresis, and visualized with colloidal Coomassie blue. The target lane from gels were prepared for analysis by LC-MS/MS. The MS spectrum was acquired using an Orbitrap Fusion LUMOS mass spectrometer (Thermo Fisher Scientific) connected to an Easy-nLC 1200 via an Easy Spray (Thermo Fisher Scientific). The MS analysis were conducted using the DAVID Bioinformatics database.

**Immunoprecipitation.** After co-cultured with sEVs-FLAG-LRG1 for 48h, cells were harvested, lysed, and briefly sonicated at 4°C. The supernatants (whole-cell lysates) were collected and incubated with Protein A/G PLUS-Agarose (Santa Cruz, sc-2003) at room temperature for 1h, and then incubated with anti-FLAG M2 beads (Sigma) at 4°C overnight. The precipitates were washed five times with immunoprecipitation buffer (50 mM Tris-HCl, PH 7.6, 150 mM NaCl, 1mM EDTA, 1% NP-40, 1 mM PMSF, and 1x protease inhibitor cocktail (Calbiochem)), boiled in sample buffer and subjected to Western blot analysis.

**Immunofluorescence.** BMDMs were seeded on coverslips in 24-well plates overnight. Treated with RANKL and GFP-labeled LRG1-sEVs for 48 hours, cells were rinsed with PBS for three

times and fixed in 4% paraformaldehyde at room temperature for 10min. Next, coverslips were rinsed in PBS for three times and permeabilized in methanol at 4°C for 10min. Then, coverslips were rinsed in PBS for three times and blocked in 1% bovine serum albumin (BSA) at room temperature for 1 h. Target protein p65 location were detected by incubating with primary antibodies (Cell Signaling Technology, 1:100) overnight at 4°C in a humid chamber. After washing three times, secondary antibodies (Texas-FITC tagged) were applied in a 1:200 dilution in staining buffer for 1h at 37 °C in a humid chamber. Then washed and coverslips were mounted with Vector shield with 4',6-diamidino-2-phenylindole (DAPI; Vector Laboratories, CA), and analyzed on a Nikon Laser Confocal Scanning Microscope.

**Primary cultures of human peripheral blood mononuclear cells (PBMCs).** Human peripheral blood mononuclear cells were isolated from healthy donors by Ficoll gradient centrifugation. Informed consent was obtained from all donors. PBMCs were cultured in α-MEM with 10% FBS (Sigma), 1% GlutaMAX™ Supplement (Thermo Fisher) and 30 ng/ml human CSF-1 (Sino Biological, Inc, 11792-H08Y) and incubated in a humidified atmosphere at 37℃ and 5% $CO_2$. For osteoclastogenesis, $5\times10^5$ PBMCs were seeded in a 12-well plate, after 48 h, cells were stimulated with 50 ng/ml human RANKL (R&D, 6449–TEC-010) and 30 ng/ml human CSF-1 for 8-10 days. Medium was changed every 2 days. Osteoclasts were fixed and stained using the TRAP-staining kit (Sigma-Aldrich, 387A-1KT).

**Patient blood samples and Human bone mineral densities (BMD).** Patient blood samples were collected from 120 patients aged 60-70 years between 2018 and 2021 at Shanghai General Hospital, Shanghai, China. Bone mineral densities (BMD) were measured by dual-energy x-ray absorptiometry. BMD was analyzed in three categories: normal, osteopenia, and osteoporosis, based on the WHO T-score classification (Osteoporosis was defined as T-score below -2.5, osteopenia was defined as T-score between -1.0 and -2.5and T-score higher than -1.0 normal). All participants are patients who need spine surgery, meet the clinical indications for bone mineral density measurement. And all of them underwent standardized preoperative examinations and had no history of chronic liver disease, diabetes, tumor or other organ diseases. The study was approved by the Ethics Committee of Shanghai General Hospital, Shanghai Jiaotong University School of Medicine, and conducted in accordance with ethical principles of the World Medical Association and declaration of Helsinki. Informed consent was

679 written by all patients prior to this study.

680 **Statistical Analysis.** Experiments were performed in three times and data are presented as the
681 mean ± standard deviation (SD), and the graphs and diagrams were generated by GraphPad
682 Prism. Differences between two groups or among multiple groups were analyzed by using the
683 Student t-test. p value $<0.05$ was defined as statistically significant.

684

685 ## Data availability

686 The data that support the findings of this study are available from the authors upon reasonable
687 request.

688

# References


1. Schuit, S.C*., et al.* Fracture incidence and association with bone mineral density in elderly men and women: the Rotterdam Study. *Bone* **34**, 195-202 (2004).
2. Rachner, T.D., Khosla, S. & Hofbauer, L.C. Osteoporosis: now and the future. *Lancet* **377**, 1276-1287 (2011).
3. Weske, S*., et al.* Targeting sphingosine-1-phosphate lyase as an anabolic therapy for bone loss. *Nat Med* **24**, 667-678 (2018).
4. Boyle, W.J., Simonet, W.S. & Lacey, D.L. Osteoclast differentiation and activation. *Nature* **423**, 337-342 (2003).
5. Asagiri, M. & Takayanagi, H. The molecular understanding of osteoclast differentiation. *Bone* **40**, 251-264 (2007).
6. Park, J.H., Lee, N.K. & Lee, S.Y. Current Understanding of RANK Signaling in Osteoclast Differentiation and Maturation. *Mol Cells* **40**, 706-713 (2017).
7. Kim, J.H. & Kim, N. Regulation of NFATc1 in Osteoclast Differentiation. *J Bone Metab* **21**, 233-241 (2014).
8. Yu, M*., et al.* Ovariectomy induces bone loss via microbial-dependent trafficking of intestinal TNF+ T cells and Th17 cells. *J Clin Invest* **131**(2021).
9. Guarino, M*., et al.* Osteoporosis across chronic liver disease. *Osteoporos Int* **27**, 1967-1977 (2016).
10. DeLuca, H.F. Vitamin D: Historical Overview. *Vitam Horm* **100**, 1-20 (2016).
11. Watt, M.J., Miotto, P.M., De Nardo, W. & Montgomery, M.K. The Liver as an Endocrine Organ—Linking NAFLD and Insulin Resistance. *Endocrine Reviews* **40**, 1367-1393 (2019).
12. Ehnert, S*., et al.* Hepatic Osteodystrophy-Molecular Mechanisms Proposed to Favor Its Development. *Int J Mol Sci* **20**(2019).
13. Wang, X., Wei, W., Krzeszinski, J.Y., Wang, Y. & Wan, Y. A Liver-Bone Endocrine Relay by IGFBP1 Promotes Osteoclastogenesis and Mediates FGF21-Induced Bone Resorption. *Cell Metab* **22**, 811-824 (2015).
14. Kalluri, R. & LeBleu, V.S. The biology, function, and biomedical applications of exosomes. *Science* **367**(2020).
15. Sung, S., Kim, J. & Jung, Y. Liver-Derived Exosomes and Their Implications in Liver Pathobiology. *Int J Mol Sci* **19**(2018).
16. Qin, W. & Dallas, S.L. Exosomes and Extracellular RNA in Muscle and Bone Aging and Crosstalk. *Curr Osteoporos Rep* **17**, 548-559 (2019).
17. Yin, P*., et al.* Exosome-Mediated Genetic Information Transfer, a Missing Piece of Osteoblast-Osteoclast Communication Puzzle. *Front Endocrinol (Lausanne)* **8**, 336 (2017).
18. Wang, Y., Yang, J., Hong, T., Chen, X. & Cui, L. SIRT2: Controversy and multiple roles in

disease and physiology. *Ageing Res Rev* **55**, 100961 (2019).
19. He, M.*, et al.* An Acetylation Switch of the NLRP3 Inflammasome Regulates Aging-Associated Chronic Inflammation and Insulin Resistance. *Cell Metab* **31**, 580-591.e585 (2020).
20. Zhang, Y.*, et al.* SIRT2-mediated deacetylation and deubiquitination of C/EBPβ prevents ethanol-induced liver injury. *Cell Discov* **7**, 93 (2021).
21. Wang, X.*, et al.* LRG1 promotes angiogenesis by modulating endothelial TGF-β signalling. *Nature* **499**, 306-311 (2013).
22. Vaquero, A.*, et al.* SirT2 is a histone deacetylase with preference for histone H4 Lys 16 during mitosis. *Genes Dev* **20**, 1256-1261 (2006).
23. Wang, R.H.*, et al.* Negative reciprocal regulation between Sirt1 and Per2 modulates the circadian clock and aging. *Sci Rep* **6**, 28633 (2016).
24. Li, D.*, et al.* Osteoclast-derived exosomal miR-214-3p inhibits osteoblastic bone formation. *Nat Commun* **7**, 10872 (2016).
25. Luo, J.*, et al.* LGR4 is a receptor for RANKL and negatively regulates osteoclast differentiation and bone resorption. *Nat Med* **22**, 539-546 (2016).
26. Jing, Y.*, et al.* SIRT2 deficiency prevents age-related bone loss in rats by inhibiting osteoclastogenesis. *Cell Mol Biol (Noisy-le-grand)* **65**, 66-71 (2019).
27. Sun, H., Sherrier, M. & Li, H. Skeletal Muscle and Bone - Emerging Targets of Fibroblast Growth Factor-21. *Front Physiol* **12**, 625287 (2021).
28. Lu, K.*, et al.* Defects in a liver-bone axis contribute to hepatic osteodystrophy disease progression. *Cell Metab* **34**, 441-457.e447 (2022).
29. Jann, J., Gascon, S., Roux, S. & Faucheux, N. Influence of the TGF-β Superfamily on Osteoclasts/Osteoblasts Balance in Physiological and Pathological Bone Conditions. *Int J Mol Sci* **21**(2020).
30. Crane, J.L. & Cao, X. Bone marrow mesenchymal stem cells and TGF-β signaling in bone remodeling. *J Clin Invest* **124**, 466-472 (2014).
31. Yakar, S.*, et al.* Circulating levels of IGF-1 directly regulate bone growth and density. *J Clin Invest* **110**, 771-781 (2002).
32. Melis, D.*, et al.* Reduced bone mineral density in glycogen storage disease type III: evidence for a possible connection between metabolic imbalance and bone homeostasis. *Bone* **86**, 79-85 (2016).
33. Gallego-Rojo, F.J.*, et al.* Bone mineral density, serum insulin-like growth factor I, and bone turnover markers in viral cirrhosis. *Hepatology* **28**, 695-699 (1998).
34. Nakchbandi, I.A. & van der Merwe, S.W. Current understanding of osteoporosis associated with liver disease. *Nat Rev Gastroenterol Hepatol* **6**, 660-670 (2009).
35. Nakchbandi, I.A. Osteoporosis and fractures in liver disease: relevance, pathogenesis and therapeutic implications. *World J Gastroenterol* **20**, 9427-9438 (2014).

36. Song, Y., Liu, J., Zhao, K., Gao, L. & Zhao, J. Cholesterol-induced toxicity: An integrated view of the role of cholesterol in multiple diseases. *Cell Metab* **33**, 1911-1925 (2021).
37. Ghosh, S. & Karin, M. Missing pieces in the NF-kappaB puzzle. *Cell* **109 Suppl**, S81-96 (2002).
38. Xie, Z*., et al.* A Novel Diterpenoid Suppresses Osteoclastogenesis and Promotes Osteogenesis by Inhibiting Ifrd1-Mediated and IκBα-Mediated p65 Nuclear Translocation. *J Bone Miner Res* **33**, 667-678 (2018).
39. Tokunaga, T*., et al.* TGFβ1 Regulates Human RANKL-Induced Osteoclastogenesis via Suppression of NFATc1 Expression. *Int J Mol Sci* **21**(2020).
40. Ahn, K.S*., et al.* Salinosporamide A (NPI-0052) potentiates apoptosis, suppresses osteoclastogenesis, and inhibits invasion through down-modulation of NF-kappaB regulated gene products. *Blood* **110**, 2286-2295 (2007).
41. Moreno, R., Sobotzik, J.M., Schultz, C. & Schmitz, M.L. Specification of the NF-kappaB transcriptional response by p65 phosphorylation and TNF-induced nuclear translocation of IKK epsilon. *Nucleic Acids Res* **38**, 6029-6044 (2010).
42. Ensrud, K.E. & Crandall, C.J. Osteoporosis. *Ann Intern Med* **167**, Itc17-itc32 (2017).
43. Black, D.M. & Rosen, C.J. Clinical Practice. Postmenopausal Osteoporosis. *N Engl J Med* **374**, 254-262 (2016).
44. Wakolbinger, R*., et al.* Bone microarchitecture and bone turnover in hepatic cirrhosis. *Osteoporos Int* **30**, 1195-1204 (2019).
45. Louvet, L*., et al.* Sirtuin 1 deficiency decreases bone mass and increases bone marrow adiposity in a mouse model of chronic energy deficiency. *Bone* **136**, 115361 (2020).
46. Kim, S.J*., et al.* Loss of Sirtuin 6 in osteoblast lineage cells activates osteoclasts, resulting in osteopenia. *Bone* **138**, 115497 (2020).
47. Ornstrup, M.J., Harsløf, T., Kjær, T.N., Langdahl, B.L. & Pedersen, S.B. Resveratrol increases bone mineral density and bone alkaline phosphatase in obese men: a randomized placebo-controlled trial. *J Clin Endocrinol Metab* **99**, 4720-4729 (2014).
48. Tran, P.H.L*., et al.* Exosomes and Nanoengineering: A Match Made for Precision Therapeutics. *Adv Mater* **32**, e1904040 (2020).

## Acknowledgments

We thank Junke Zheng (Shanghai Jiao Tong University School of Medicine) for discussion; Core Facility of Basic Medical Sciences, Shanghai Jiao Tong University School of Medicine for the protein LC-MS analysis. This study was funded by the National Natural Science Foundation of China (No. 92057118, 82070603); Shanghai Natural Science Foundation (19ZR1440700, 19ZR1428400); Shanghai Pujiang Program by Science and Technology Commission of Shanghai Municipality (16PJ0004679, 16PJ1405400); Medical-Industrial Interdisciplinary Research Fund of Shanghai Jiaotong University (YG2017MS02); Innovative research team of high-level local universities in Shanghai (SSMU-ZDCX20180800); Youth Science and Technology Innovation Studio of Shanghai Jiao Tong University School of Medicine (JYKCGZS8, JYKCGZS15); Practice training base for interdisciplinary innovative talents of Shanghai Jiao Tong University (SJTUJXCX-3).

## Author contributions

M.H. conceived the project, designed the experiments. Q-H.Z. supervised this work. L-S.L., Z-Y.G., E-J.H., D-F.W., Y-T.Z., W-H.G., Q.W., J-C.L., L-L.W. contributed to the acquisition and analysis of data. L-S.L. performed most experiments. Z-Y.G., E-J.H., D-F.W., Y-T.Z., W-H.G. and Q.W. conducted partial experiments. Q-H.Z., L-S.L. and E-J.H. contributed in clinical sample collection and analysis. M.H. and L-S.L. analyzed data. M.H. and L-S.L. wrote the manuscript. All authors discussed the results and commented on the paper.

## Competing interests

The authors declare no competing interests.

817 Address correspondence to: Ming He, Department of Pathophysiology, Key Laboratory of Cell
818 Differentiation and Apoptosis of Ministry of Education, Shanghai Frontiers Science Center of
819 Cellular Homeostasis and Human Diseases, Shanghai Jiao Tong University School of Medicine,
820 No. 280, South Chong Qing Road, Shanghai 200025, China. E-mail: heming@shsmu.edu.cn;
821 Qinghua Zhao, Department of Orthopedics, Shanghai General Hospital, Shanghai Jiao Tong
822 University School of Medicine, No. 100, Hai Ning Road, Shanghai 200080, China. E-mail:
823 qinghua.zhao@shgh.cn.

## Figures and Figure Legends.

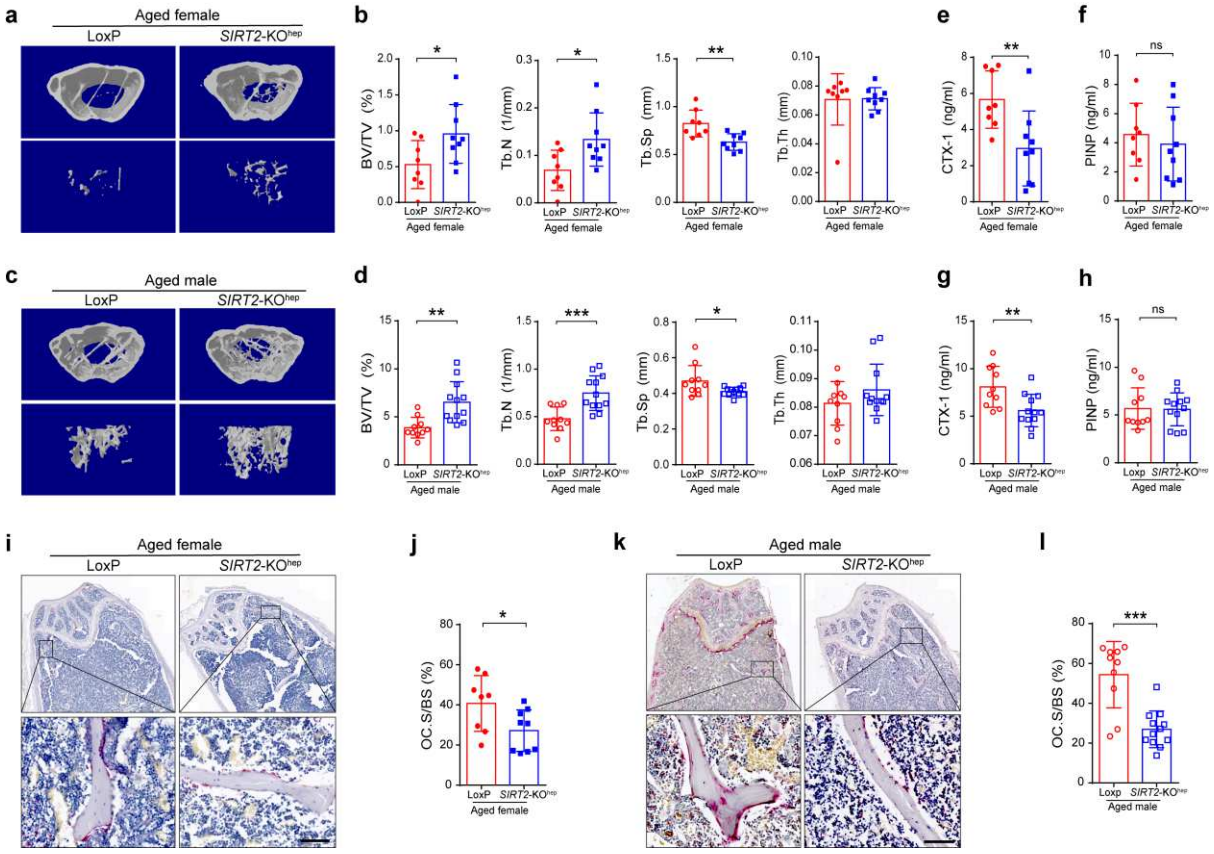


**Fig.1 Hepatocyte-specific *SIRT2* knockout prevents age-related bone loss with less active osteoclastogenesis. (a)** Represented images of 3D restoration and **(b)** quantification of trabecular BV/TV, Tb.N., Tb.Sp. and Tb.Th. of distal femur of the aged female LoxP and *SIRT2*-KO$^{hep}$ mice (18 months of age), as measured by micro-CT (n= 8, LoxP mice and n=9, *SIRT2*-KO$^{hep}$ mice). **(c)** Represented images of 3D restoration and **(e)** quantification of trabecular BV/TV, Tb.N., Tb.Sp. and Tb.Th. of distal femur of the aged male LoxP and *SIRT2*-KO$^{hep}$ mice (18 months of age), as measured by micro-CT (n= 10, LoxP mice and n=12, *SIRT2*-KO$^{hep}$ mice). **(e, g)** Plasma CTX-1 and **(f, h)** PINP in aged female and male LoxP and *SIRT2*-KO$^{hep}$ mice were detected by ELISA. **(i, k)** TRAP staining on paraffin-embedded femur sections in aged female and male LoxP and *SIRT2*-KO$^{hep}$ mice (scale bar, 100 μm). **(j, l)** Quantification of osteoclast surface/bone surface ratios (Oc.S/BS) are shown on the right. Data are presented as mean ± SD. $^{*}p < 0.05$, $^{**}p < 0.01$, $^{***}p < 0.001$.

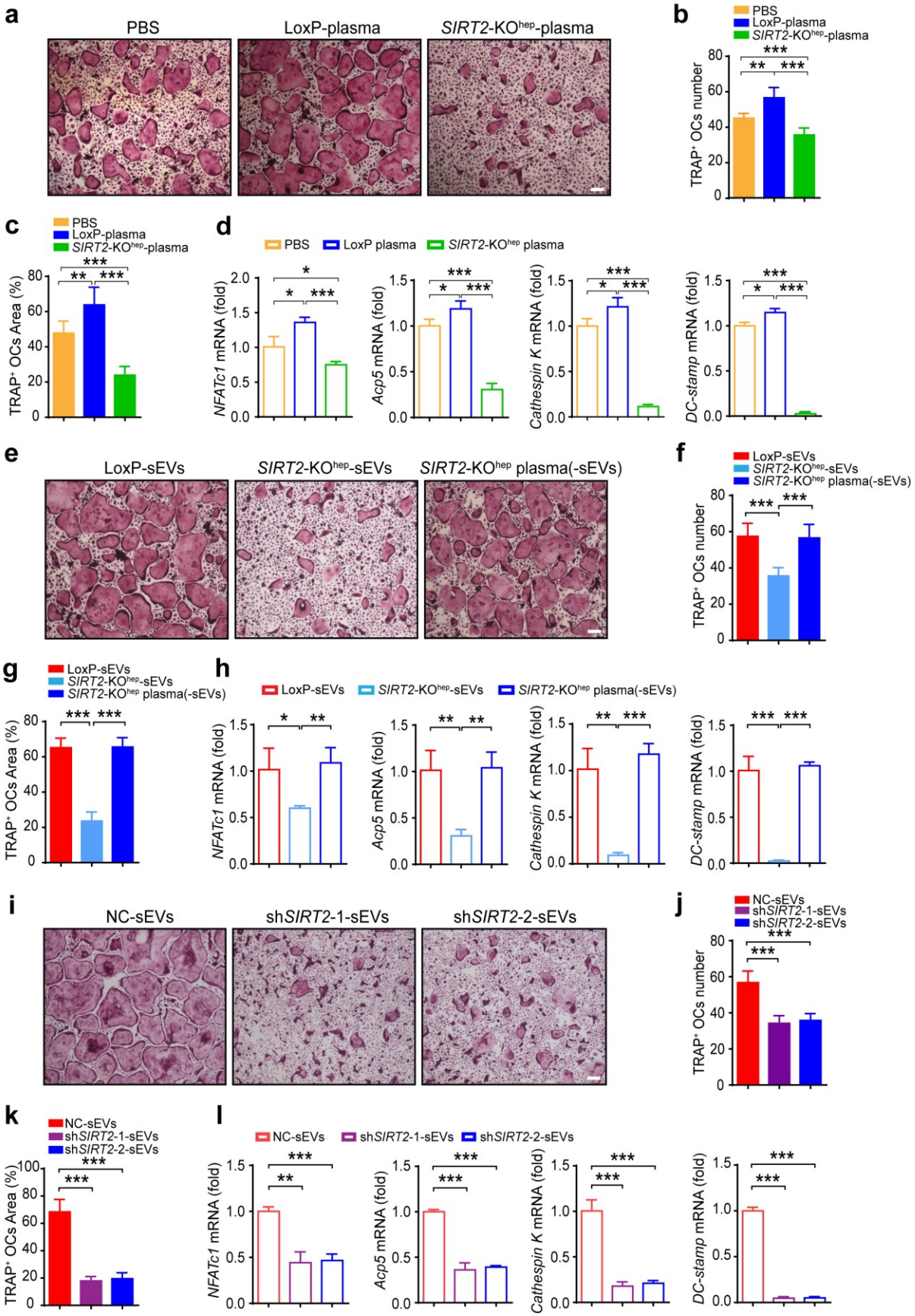


**Fig.2 Aged *SIRT2*$^{-/-}$ hepatocyte-derived sEVs inhibit osteoclastogenesis.** Bone marrow-derived monocytes (BMDMs) were isolated and cultured with murine M-CSF and RANKL

stimulation for 7 days to generate osteoclasts, combined with the corresponding treatments. **(a)** Representative TRAP staining images of osteoclasts administered with the plasma of aged LoxP or *SIRT2*-KO$^{hep}$ male mice (LoxP-plasma or *SIRT2*-KO$^{hep}$-plasma) (scale bar, 200 μm). **(b)** Number and **(c)** area of multi-nucleated TRAP$^{+}$ cells with indicated treatment were measured respectively. **(d)**The osteoclast-specific genes *NFATc1, Acp5, Cathespin K,* and *DC-stamp* mRNA levels in LoxP-plasma or *SIRT2*-KO$^{hep}$-plasma-treated osteoclasts were measured by real-time PCR. **(e)** Representative TRAP staining images of osteoclasts treated with the sEVs derived from LoxP plasma or *SIRT2*-KO$^{hep}$ plasma (LoxP-sEVs or *SIRT2*-KO$^{hep}$-sEVs), as well as with *SIRT2*-KO$^{hep}$-plasma depleted sEVs (*SIRT2*-KO$^{hep}$-plasma(-sEVs)) (scale bar, 200 μm). **(f)** Number and **(g)** area of multi-nucleated TRAP$^{+}$ cells with indicated treatment were measured. **(h)** The mRNA expression of osteoclast-specific genes in the corresponding treated-osteoclasts was measured by real-time PCR. **(i)** Representative TRAP staining images of osteoclasts treated with the sEVs derived from control AML12 hepatocytes (NC-sEVs) or *SIRT2*-knockdown AML12 hepatocytes (sh*SIRT2*-1-sEVs or sh*SIRT2*-2-sEVs) (scale bar, 200 μm). **(j)** Number and **(k)** area of multi-nucleated TRAP$^{+}$ cells with indicated treatment were measured. **(l)** The mRNA expression of osteoclast-specific genes in the corresponding treated-osteoclasts was measured by real-time PCR. Data are presented as mean ± SD. $^{*}p < 0.05$, $^{**}p < 0.01$, $^{***}p < 0.001$.

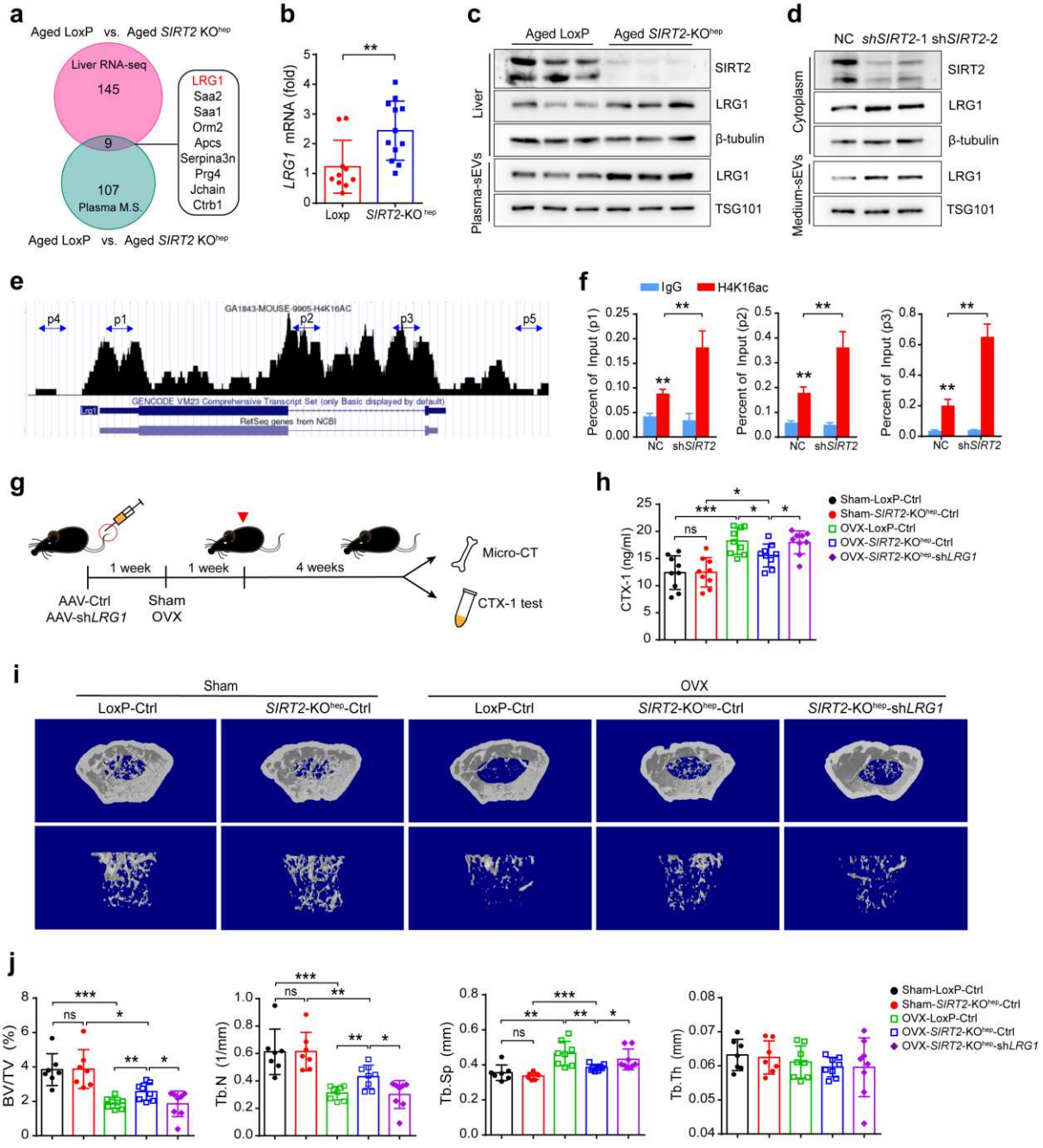


**Fig.3 *SIRT2*-KO$^{hep}$ prevents against OVX-induced bone loss through up-regulating LRG1 expression in hepatocytes. (a)** Venn diagram showing the overlap numbers of *SIRT2*-KO$^{hep}$-regulated plasma proteins by Mass spectra and *SIRT2*-KO$^{hep}$-regulated hepatic mRNAs by RNA-seq in aged mice (18 months of age). **(b)** *LRG1* mRNA expression in the livers of aged LoxP and *SIRT2*-KO$^{hep}$mice measured by real-time PCR. **(c)** Western blot analysis of LRG1 protein expression in the liver and plasma-sEVs of aged LoxP and *SIRT2*-KO$^{hep}$ mice. **(d)** Western blot analysis of LRG1 protein expression in the cytoplasm and supernatant-derived sEVs of NC and sh*SIRT2* AML12 hepatocytes. **(e)** Schematic view of enrichment of H4K16ac on LRG1 promoter

region from ChIP-seq data from Cistrome DB Toolkit. **(f)** ChIP analysis showing the enrichment of H4K16ac at the LRG1 proximal promoter region in NC and sh*SIRT2* AML12 hepatocytes using the primers p1, p2 and p3. **(g)** The experimental procedure for hepatocyte-specific *LRG1* knockdown by AAV8 virus. LoxP and *SIRT2*-KO$^{hep}$ mice (12 weeks of age) were given tail injections with $2\times10^{11}$ viral particles of either AAV8-sh*LRG1* or Ctrl vector 7 days before OVX to maximize the viral expression and knockdown efficiency. The real-time observation of gene expression was performed by BLI at 14$^{th}$ day after viral injection. Mice were sacrificed at five weeks after OVX for CTX-1 and bone mass test. **(h)** Plasma CTX-1was detected by ELISA. **(i)** Represented images of 3D restoration and **(j)** quantification of trabecular BV/TV, Tb.N., Tb.Sp. and Tb.Th. of distal femur of the indicated group mice, as measured by micro-CT. Data are presented as mean ± SD. $^{*}p < 0.05$, $^{**}p < 0.01$, $^{***}p < 0.001$.

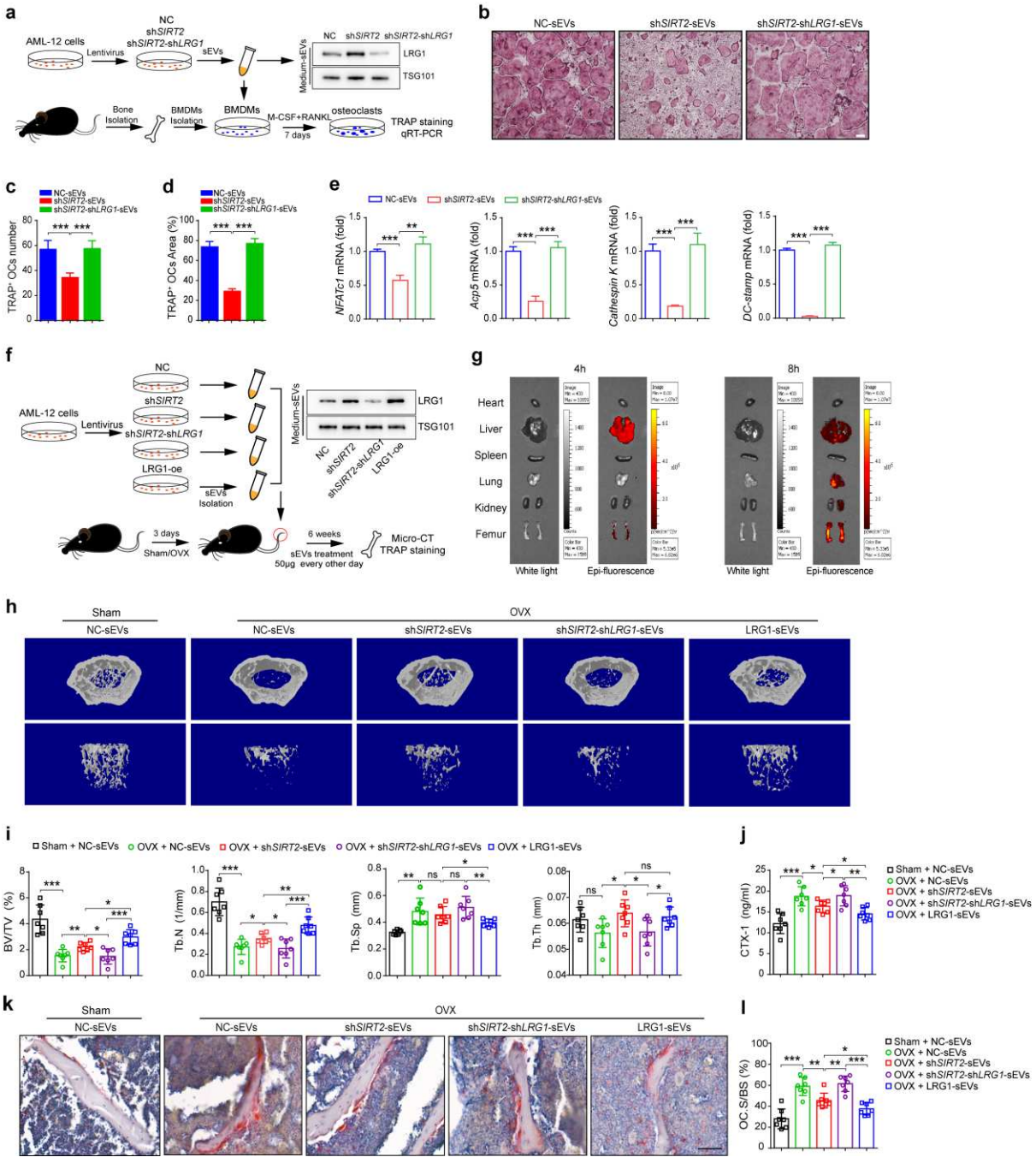


881

882 **Fig.4 Hepatocyte-derived sEVs-LRG1 mediates the protection of *SIRT2*-KO$^{hep}$ against**
883 **osteoclastogenesis and bone loss. (a)** Schema of BMDM treatment with sEVs. The sEVs were
884 purified from the supernatant of sh*SIRT2*-AML12 cells infected with Ctrl or sh*LRG1* lentiviral
885 vectors. sEVs-LRG1 protein expression was analyzed by Western blot. The isolated primary
886 BMDMs were co-cultured with each set of transduced sEVs and murine M-CSF/RANKL stimulation
887 for 7 days to generate osteoclasts and followed TRAP staining and real-time PCR test. **(b)** TRAP
888 staining of osteoclasts treated with NC-sEVs or sh*SIRT2*-sEVsor sh*SIRT2*-sh*LRG1*-sEVs (scale
889 bar, 200 μm). **(c)** Number and **(d)** area of multi-nucleated TRAP$^{+}$ cells with indicated treatment

were measured. **(e)** The mRNA expression of osteoclast-specific genes in the corresponding treated-osteoclasts was measured by real-time PCR. **(f)** The experimental procedure for sEVs treatment *in vivo*. C57BL/6 J mice were consecutively intravenously injected with the NC-sEVs, sh*SIRT2*-sEVs and sh*SIRT2*-sh*LRG1*-sEVs (50μg per mouse, every other day) 3 days after OVX. Micro-CT and the TRAP staining were performed 6 weeks after the first injection. **(g)** Representative biophotonic images of the tissue distribution of fluorescence signal in mice at 4 and 8h after intravenous injection ofPKH26-labelled sEVs isolated from the supernatant of AML-12 cells. **(h)** Represented images of 3D restoration and **(i)** quantification of trabecular BV/TV, Tb.N., Tb.Sp. and Tb.Th. of distal femur of the indicated group mice, as measured by micro-CT. **(j)** Plasma CTX-1 in each group was detected by ELISA. **(k)** TRAP staining on paraffin-embedded femur sections in each group after corresponding sEVs treatment (scalebar, 100 μm). **(l)** Quantification of Oc.S/BS is shown on the right. Data are presented as mean ± SD. $^{*}p < 0.05$, $^{**}p < 0.01$, $^{***}p < 0.001$.

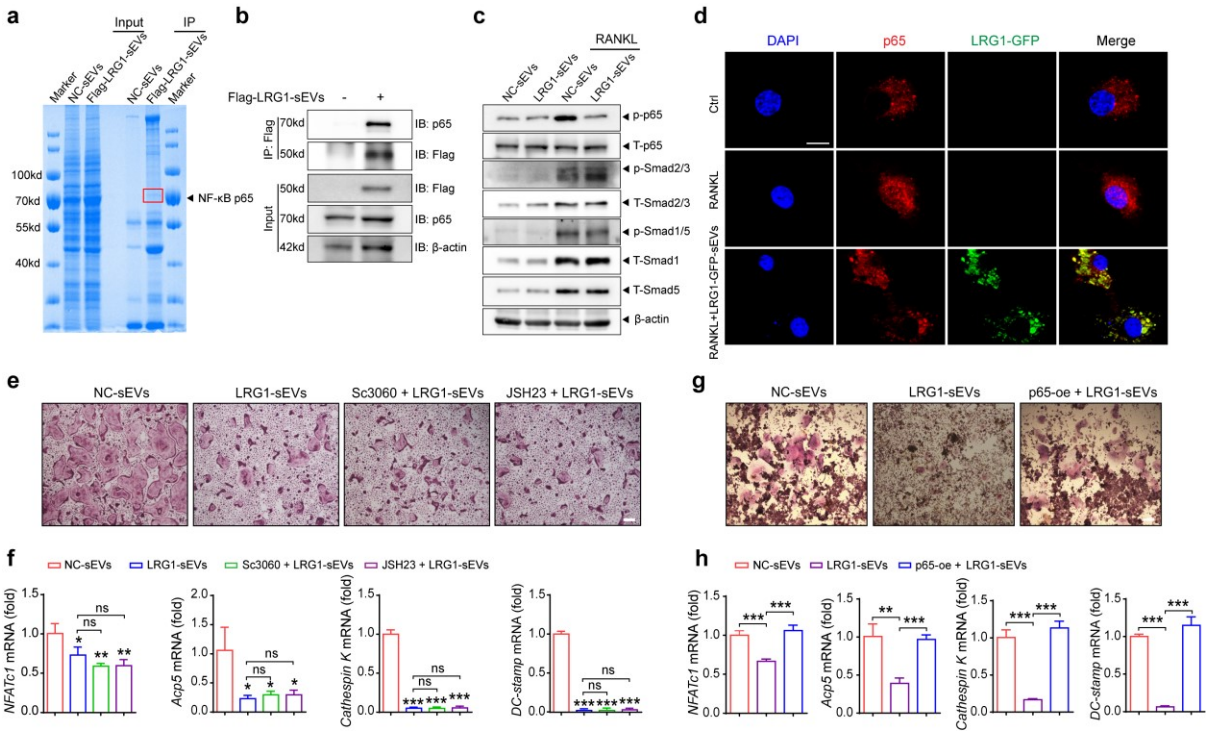


**Fig.5 Hepatocyte-derived sEVs-LRG1 inhibits osteoclastogenesis by repressing RANKL-induced NF-κB p65 nuclear translocation. (a)** Western blot of the hepatocyte-derived sEVs-LRG1 binding proteins identified by immunoprecipitation (IP) assays in BMDMs, followed by LC-MS. **(b)** Endogenous sEVs-LRG1-NF-κB p65 interaction was analyzed by the amount of NF-κB p65 co-immunoprecipitated with the sEVs-Flag-LRG1 in primary BMDMs. **(c)** Western blot analysis of phosphorylation of p65 and the activities of TGF-β signaling in osteoclasts treated with LRG1-sEVs. **(d)** Immunofluorescence analysis of p65 (red) location in RANKL-induced BMDMs treated with LRG1-GFP-sEVs (green) (scale bar, 20 μm). **(e)** TRAP staining of osteoclasts treated with LRG1-sEVs and the inhibitors of p65 nuclear translocation, Sc-3060(10μM) and JSH-23(6μM) (scale bar, 200 μm). **(f)** The mRNA expression of osteoclast-specific genes in each group osteoclasts were measured by real-time PCR. **(g)** TRAP staining of RAW264.7 cells overexpressed p65 and treated with LRG1-sEVs (scale bar, 200 μm). **(h)** The mRNA expression of osteoclast-specific genes in each indicated group osteoclasts were measured by real-time PCR. Data are presented as mean ± SD. $^{*}p < 0.05$, $^{**}p < 0.01$, $^{***}p < 0.001$.

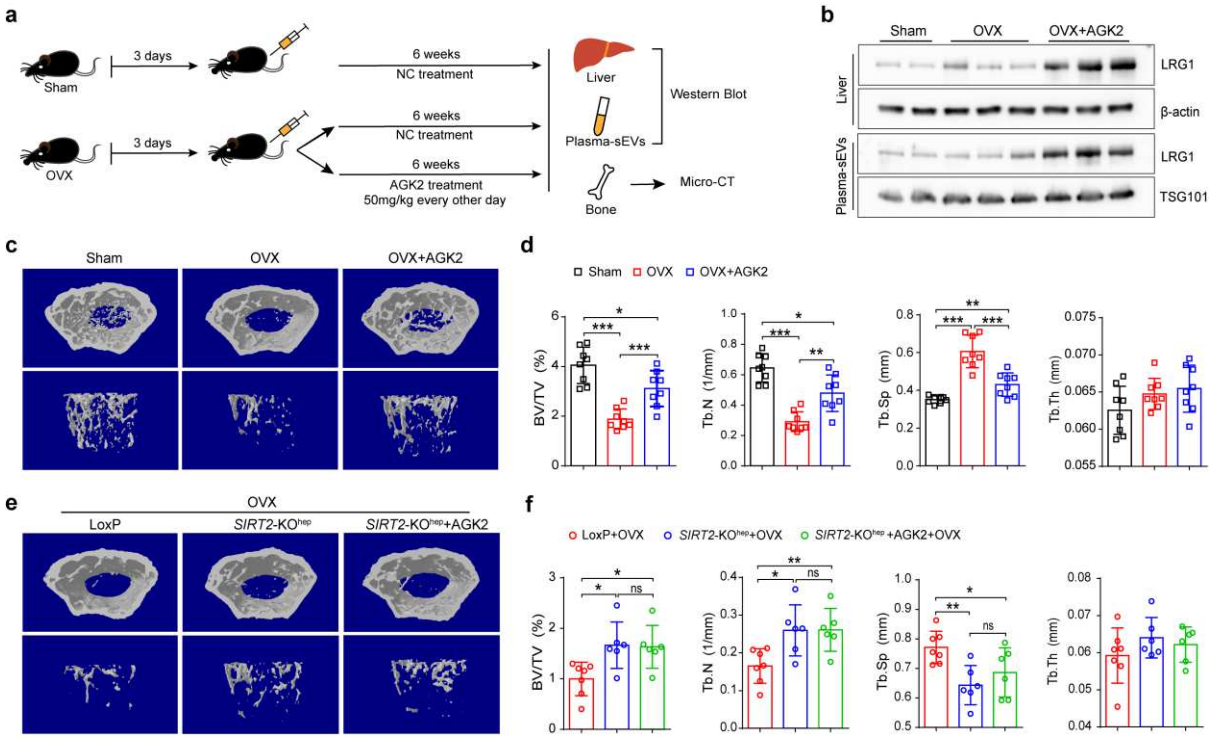


**Fig.6 SIRT2 inhibitor AGK2 significantly suppresses OVX-induced bone loss *in vivo*. (a)** The experimental procedure for AGK2 treatment on OVX mouse model. **(bc)** Western blot analysis of LRG1 protein expression in the livers and plasma-sEVs of OVX C57BL/6 J mice treated with AGK2. **(c)** Represented images of 3D restoration and **(d)** quantification of trabecular BV/TV, Tb.N., Tb.Sp. and Tb.Th. of distal femur of the OVX C57BL/6 J mice after 6-week intraperitoneal injection of AGK2 (50mg/kg, every other day), as measured by micro-CT. **(e)** Micro-CT analysis of 3D restoration and **(f)** quantification of trabecular BV/TV, Tb.N., Tb.Sp. and Tb.Th. of distal femur of the OVX *SIRT2*-KO$^{hep}$ mice after 6-week treatment of AGK2. Data are presented as mean ± SD. $^{*}p < 0.05$, $^{**}p < 0.01$, $^{***}p < 0.001$.

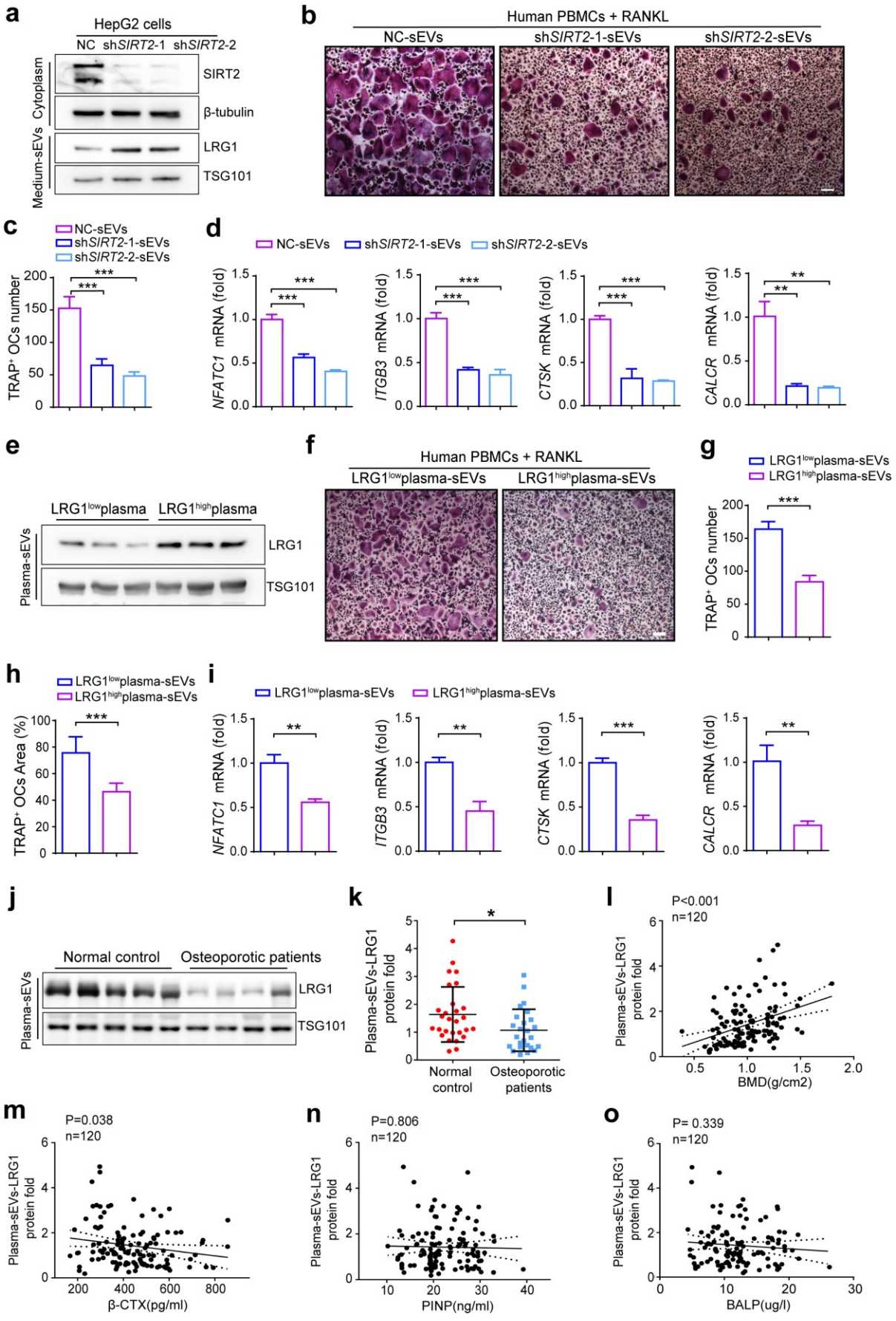


**Fig.7 Hepatocyte-derived sh*SIRT2*-sEVs or Human LRG1$^{high}$ plasma-sEVs inhibit human**

**osteoclast differentiation and plasma-sEVs-LRG1 inversely correlates with bone resorption in patients. (a)** Western blot analysis of LRG1 protein expression in the cytoplasm and sEVs derived from *SIRT2* knockdown (sh*SIRT2*) HepG2 human hepatocytes. **(b)** Representative TRAP staining images of human peripheral blood mononuclear cells (PBMCs) cultured with RANKL and sEVs drived from the supernatant of control and sh*SIRT2* HepG2 cells (NC-sEVs, sh*SIRT2*-1-sEVs, sh*SIRT2*-2-sEVs) (scale bars, 200 μm). **(c)** Number of multi-nucleated $TRAP^+$ cells with indicated treatment was measured. **(d)** The mRNA expression of osteoclast-specific genes in the corresponding treated-osteoclasts was measured by real-time PCR. **(e)** Western blot analysis of LRG1 protein expression in the sEVs derived from LRG1 high or low expression plasma. **(f)** Representative TRAP staining images of human PBMCs cultured with RANKL and sEVs drived from three LRG1 high expression human plasma or three LRG1 low expression human plasma ($LRG1^{low}$ plasma-sEVs, $LRG1^{high}$ plasma-sEVs) (scale bars, 200 μm). **(g)** Number and **(h)** area of multi-nucleated $TRAP^+$ cells. **(i)** The mRNA expression of osteoclast-specific genes measured by real-time PCR. **(j)** Western blot analysis of the protein expression of plasma-sEVs-LRG1 from female normal control (BMD T score of Lumbar spine is greater than -1) and osteoporotic patients (BMD T score of Lumbar spine is less than -2.5). **(k)** Plots of protein expression of plasma-sEVs-LRG1 in female normal control (n=28) and osteoporotic patient group (n=25). Association between human plasma-sEVs-LRG1 expression and BMD **(l)**, bone resorption marker β-CTX **(m)** and bone formation markers PINP **(n)** and BALP **(o)** in 120 human subjects of both sexes (females, n=84 and males, n=36). Statistical significance was determined by two-tailed Student's t test **(k)**, All results in **l-o** are from multivariable linear regression analyses. Data are presented as mean ± SD. $^{*}p < 0.05$, $^{**}p < 0.01$, $^{***}p < 0.001$.

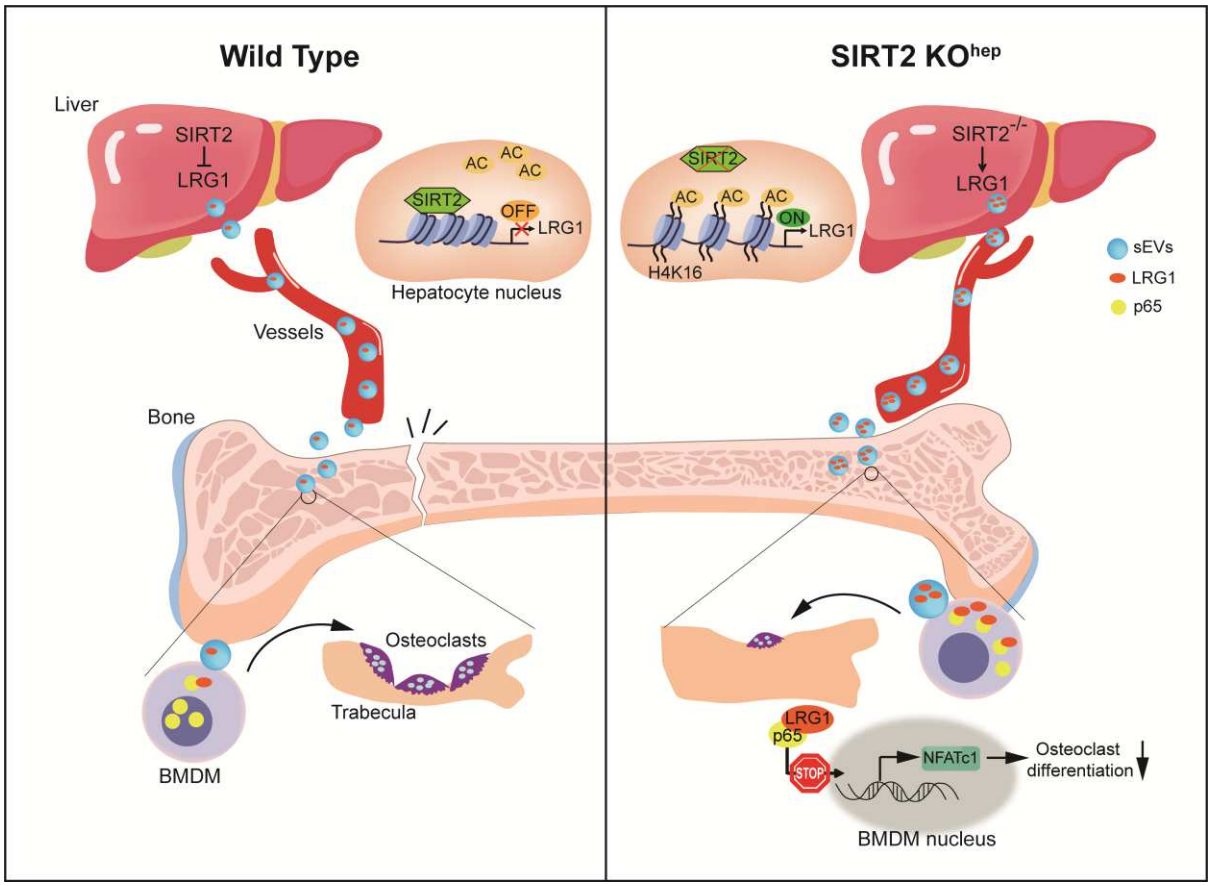


**Fig.8 A working model of the novel liver-bone communication.** Hepatocyte SIRT2 regulates pro-osteoclastic signaling of NF-κB p65 in osteoclasts through sEVs-LRG1. Up-regulated LRG1 protein in SIRT2$^{-/-}$ hepatocyte transferred into osteoclasts through sEVs acts as a brake on pro-osteoclastic activity to maintain aged and postmenopausal bone homeostasis. The inter-organ action of SIRT2-sEVs-LRG1-NF-κB-NFATc1 axis may be a promising therapeutic target in primary osteoporosis.

# Supplementary Files

This is a list of supplementary files associated with this preprint. Click to download.

- NMsupplemental.pdf